Post-print of: Koziel, S. and Bekasiewicz, A., Fast multi-objective design optimization of microwave and antenna structures using data-driven surrogates and domain segmentation, Engineering Computations, Vol. 37 No. 2 (2019) pp. 753-788 https://doi.org/10.1108/EC-01-2019-0004

Fast Multi-Objective Design Optimization of Microwave and Antenna Structures Using Data-Driven Surrogates and Domain Segmentation

Keywords: Computer-aided design (CAD), microwave and antenna design, multi-objective optimization, surrogate models, evolutionary algorithms, domain segmentation.

Structured Abstract

Purpose

Strategies and algorithms for expedited design optimization of microwave and antenna structures in multi-objective setup are investigated.

Design/methodology/approach

Formulation of the multi-objective design problem oriented towards execution of the population-based metaheuristic algorithm within the segmented search space is investigated. Described algorithmic framework exploit variable fidelity modeling, physics- and approximation-based representation of the structure, as well as model correction techniques. The considered approach is suitable for handling various problems pertinent to design of microwave and antenna structures. Numerical case studies are provided demonstrating feasibility of the segmentation-based framework for design of real-world structures in setups with two and three objectives.

Findings

Formulation of appropriate design problem enables identification of the search space region containing Pareto front which can be further divided into a set of compartments characterized by small combined volume. Approximation model of each segment can be constructed using a small number of training samples and then optimized, at a negligible computational cost, using population-based metaheuristics. Introduction of segmentation mechanism to multi-objective design framework is important to facilitate low cost optimization of many-parameter structures represented by numerically expensive computational models. Further reduction of the design cost can be achieved by enforcing equal-volumes of the search space segments.

Research limitations/implications

The study summarizes recent advances in low-cost multi-objective design of microwave and antenna structures. The investigated techniques exceed capabilities of conventional design approaches involving direct evaluation of physics-based models for

determination of trade-offs between the design objectives, particularly in terms of reliability and reduction of the computational cost. Studies on scalability of segmentation mechanism indicate that computational benefits of the approach decrease with the number of search space segments.

Originality/value

The proposed design framework proved useful for rapid multi-objective design of microwave and antenna structures characterized by complex and multi-parameter topologies, which is extremely challenging when using conventional methods driven by population-based metaheuristics algorithms. To our knowledge, this is the first work that summarizes segmentation-based approaches to multi-objective optimization of microwave and antenna components.

Abstract

The paper addresses fast multi-objective optimization of computationally-expensive simulation models of microwave and antenna structures. In order to reduce the cost of the design process, a surrogate-assisted approach is adopted along with utilization of variable-fidelity simulation models. The initial Pareto set is obtained by optimizing an auxiliary kriging surrogate using a multi-objective evolutionary algorithm. The final Pareto set is then generated through a refinement procedure that involves response correction. In the above algorithm, acquisition of the training data for surrogate model construction is one of the main contributors to the overall optimization cost. Here, it is limited by introducing design space segmentation in which a relevant part of the search space is identified by means of single-objective optimization runs and subsequently covered by a set of adjacent compartments with individual surrogate models established within them. Segmentation permits significant reduction of the number of training points necessary to build a reliable surrogate and, consequently, the overall optimization cost. The presented technique is demonstrated using several real-world structures and compared to a state-of-the-art method that does not rely on domain segmentation. Thorough the work, the analysis of the algorithm performance, as well as its extension for more than two objectives are also discussed. Numerical results are supported by experimental validation of the selected designs.

1. Introduction

Practical design optimization of contemporary microwave and antenna structures is a challenging process. Due to reliability requirements, it heavily relies on full-wave electromagnetic (EM) simulation models that may be computationally expensive [1], [2]. If certain environmental interactions need to be accounted for (e.g., the presence of connectors [3], housing [4], installation fixtures [5]), the simulation time can be as long as several minutes but even a few hours for electrically large devices [6], [7]. Furthermore, optimum designs can only be obtained by simultaneous adjustment of all relevant geometry and/or material parameters and the typical number of such parameters for individual components is between ten and twenty [8], [9], but it may easily become a few dozen or more for, e.g., diversity antennas or complex couplers [10], [11]. Consequently, numerical optimization of structures EM models is a very time consuming process, often prohibitive. There has been considerable research effort towards alleviating these difficulties, in particular, reducing the cost of EM-driven design processes. The methods reported in the literature involve utilization of adjoint sensitivities [12]-[15], as well as data-driven [16]-[19] and physics-based [20]-[23] surrogate models. In addition to generic techniques, the algorithms tailored to particular classes of structures, e.g., multi-band [10], [24], broadband, [3], [25], or compact [2], [4] have been proposed.

Design of modern structures requires handling of several performance parameters (e.g., impedance bandwidth [6], isolation [26], coupling [11], gain [27], efficiency [25], radiation pattern [28], axial ratio [9], pattern stability [29], pulse fidelity [29], etc.), as well as physical dimensions [1]-[15]. Maintaining small size is particularly important for space limited applications such as wireless communication [26], wearable [30], or

Internet of Things devices [31]. Various design goals are usually conflicting so that improvement over one of them normally leads to degradation of the remaining ones [9], [32]. A representative problem includes design of compact antennas, where, for a given topology of the structure, size reduction typically leads to degradation of reflection and gain responses [33]. Another example is the design of miniaturized coupler where miniaturization is achieved at a cost of narrower bandwidth [35], [36]. Thus, any realistic design is a compromise between the considered requirements. The knowledge about the best possible trade-offs (also referred to as a Pareto front [37]) is invaluable for the designer as it allows to facilitate the decision making process in the context of selecting the most appropriate structure for a particular application [38], but also identifying the optimum parameter values for given performance specifications [39]. This sort of information can be determined by means of multi-objective optimization [37], [38].

There are various techniques available for carrying out multi-objective optimization. The simplest approaches are based on aggregating design goals into scalar objective functions (weighted sum methods [37]) or by imposing (hard or soft) thresholds on certain objectives (e.g., goal attainment [40]). This permits utilization of conventional optimization techniques but only allows for finding a single Pareto-optimal design in one algorithm run [37]. By far, the most popular multi-objective optimization approaches are population-based metaheuristics, including genetic algorithms (GAs) [38], [41], particle swarm optimizers (PSO) [1], [42] differential evolution (DE) [6], [43], or firefly algorithm [44], [45], etc. Because of processing sets of candidate solutions and implementing special mechanisms such as Pareto-ranking-based selection [37] or fitness sharing [46], metaheuristics are capable of identifying the entire representations of the

Pareto set in a single algorithm run [40]. However, computational complexity of these algorithms is high. Typical costs range from a few thousands to tens of thousands of objective function evaluations [1], [27] (specific numbers are very much problem dependent). Clearly, there are cases where this is not an issue, e.g., optimization of analytical array factor models for antenna arrays [42], [47], or circuit-model-based structures [48], [49]. However, for vast majority of contemporary structures, full-wave EM analysis is required for accurate evaluation. This is when the running cost of population-based metaheuristics becomes prohibitive [1], [6].

Computationally feasible multi-objective optimization of EM simulation models of microwave/antenna structures can be realized by utilization of surrogate modeling techniques [6]. A rudimentary approach is to construct an auxiliary data-driven surrogate (using, e.g., kriging interpolation [50]) and execute a metaheuristic algorithm to generate the Pareto front [38]. Such straightforward approaches are only feasible in case of low-dimensional parameter spaces and for relatively narrow parameter ranges [51]. This is due to curse of dimensionality which makes the training data acquisition for surrogate model construction a serious bottleneck of the entire optimization process [19]. A surrogate-based optimization framework proposed in [38] also exploits kriging interpolation surrogates but constructed at the level of coarse-discretization EM simulation model. Furthermore, it relies on a space-mapping-based refinement procedure [21] to elevate the initial Pareto set to the high-fidelity EM model level (thus, to produce the final Pareto set). The method of [38] alleviates to some extent the difficulties related to high cost of training data acquisition. In [52], further steps have been made by restricting the region of the design space (without formally reducing the space

dimensionality) by considering extreme Pareto-optimal designs obtained by optimizing individual objectives (one at a time). More involved design space reduction methods have been proposed in [33] and [53], based on exploring Pareto front geometry. As a result, relatively high-dimensional cases of 20 parameters and beyond were successfully handled [33].

In [54], a design space segmentation approach has been introduced which allows for further and significant reduction of the computational cost of multi-objective antenna optimization compared to [52]. According to this methodology, the region of design space that contains the Pareto front is covered with several intervals spanned by the Pareto-optimal designs found through constrained single-objective optimization runs. The intervals still cover majority of the front yet their total volume is dramatically smaller than that of the original design space and so is the number of training samples necessary for surrogate model construction. This leads to computational benefits in terms of reducing the overall optimization cost which became more pronounced for search spaces with increased dimensionality.

In this paper, we review the segmentation concept and illustrate it through optimization of several microwave and antenna structures of various complexities. Furthermore, we investigate scalability of the method, in particular, the benefits of increasing the number of design space intervals (segments) from the point of view of reducing the size of the training data set for surrogate construction but also the additional cost of generating the intermediate points. We also propose modification of the procedure for obtaining auxiliary points which allows for generating equal-size compartments. Finally, application of the segmentation approach to optimization in tri-objective setup is

discussed. Segmentation-based design framework is comprehensively benchmarked against state-of-the art method for low-cost multi-objective optimization driven by population-based metaheuristic algorithm and numerical results obtained for selected cases are validated experimentally.

2. Surrogate-Assisted Multi-Objective Optimization with Variable-Fidelity Models

The purpose of this section is to briefly recall the surrogate-assisted optimization methodology of [52], which is a foundation of the design framework based on the space segmentation concept discussed in detail in Section 3. Here, we outline the basic components of the approach, including an initial design space reduction, surrogate model construction, identification of the initial Pareto set, as well as its refinement.

2.1. Formulation of Multi-Objective Design Task

We denote by $\boldsymbol{R}_f(\boldsymbol{x})$ a response of an accurate model of the structure under design. In practice, $\boldsymbol{R}_f(\boldsymbol{x})$ is obtained from high-fidelity EM simulations, whereas responses typically include electrical- (e.g., reflection coefficient, isolation, coupling), or field-related (e.g., gain, efficiency, radiation pattern) performance, but also structure geometry (e.g., lateral size, footprint, volume). A vector $\boldsymbol{x}$ represents designable parameters, i.e., geometry dimensions of the structure at hand.

Let $F_k(\boldsymbol{x})$, $k = 1, \ldots, N_{obj}$, represent design objectives. In case of antennas, typical objectives would be to minimize the antenna reflection over a certain frequency band of interest [52], reduce a gain variation over a frequency band (in case of wideband antennas [55]), increase efficiency [25], minimize the antenna size [26], improve axial ratio (in case of circular polarization antennas [9]), etc. For microwave circuits, the objectives

might include minimization of reflection [51], isolation [11], or coupling error for a specific frequency [34], maximization of bandwidth [11], minimization of the phase shift difference [36], etc. In practice, all performance specifications are formulated in such a way that the objectives F_k are to be minimized [6].

Assuming that $N_{obj} > 1$, any two designs $\boldsymbol{x}^{(1)}$ and $\boldsymbol{x}^{(2)}$ for which $F_k(\boldsymbol{x}^{(1)}) < F_k(\boldsymbol{x}^{(2)})$ and $F_l(\boldsymbol{x}^{(2)}) < F_l(\boldsymbol{x}^{(1)})$ for at least one pair $k \neq l$, are not commensurable which means that none is better than the other in the multi-objective sense [38], [52]. It is customary to use a Pareto dominance relation $\prec$ [37] saying that for the two designs $\boldsymbol{x}$ and $\boldsymbol{y}$, we have $\boldsymbol{x} \prec \boldsymbol{y}$ ($\boldsymbol{x}$ dominates $\boldsymbol{y}$) if $F_k(\boldsymbol{x}) < F_k(\boldsymbol{y})$ for all $k = 1, \ldots, N_{obj}$. The multi-objective optimization task is to identify a representation of a Pareto front (or a Pareto-optimal set) X_P of the design space X, such that for any $\boldsymbol{x} \in X_P$, there is no $\boldsymbol{y} \in X$ for which $\boldsymbol{y} \prec \boldsymbol{x}$ [37]. It should be noted that the methodology considered in this work is based on the assumption that the Pareto front is continuous and its shape is non-eccentric (e.g., significantly curved). Although this is not true in general, the assumption holds for a large body of design problems in microwave/antenna engineering (including the ones considered here) [6], [33], [49], [51].

2.2. Variable-Fidelity Electromagnetic Models

Direct multi-objective optimization of the high-fidelity electromagnetic model $\boldsymbol{R}_f$ of the structure at hand is impractical as elaborated on in the introduction. As explained in [38], it is advantageous to utilize an auxiliary low-fidelity model $\boldsymbol{R}_c$, which, can be obtained from circuit model simulations or coarse-mesh EM analysis. The latter involves reduction of discretization density of the structure at hand but also by introducing other

simplifications (e.g., neglecting losses, assuming perfect metal conductors [6], etc.). In practice, $\boldsymbol{R}_c$ can be made 10 to 50 times faster than $\boldsymbol{R}_f$, however, at the expense of some accuracy degradation [6]. Figure 1 shows a few examples of real-world structures and typical relationships between low- and high-fidelity model responses.

Despite the aforementioned speedup, direct multi-objective optimization is usually too expensive even at the $\boldsymbol{R}_c$ level. The methodology of [38] exploits data-driven surrogates (specifically, kriging interpolation models [50] denoted as $\boldsymbol{R}_s$) as the main tools to yield the initial approximation of the Pareto set.

2.3. Extreme Pareto-Optimal Designs. Initial Design Space Reduction

For majority of microwave and antenna structures, Pareto fronts exhibit simple geometries. This makes it possible to considerably reduce the search space by identifying the extreme Pareto optimal designs $\boldsymbol{x}_c^{*(k)}$, $k = 1, \ldots, N_{obj}$, obtained by solving single-objective problems of the form [38]

$$\boldsymbol{x}_c^{*(k)} = \arg\min_{\boldsymbol{l} \le \boldsymbol{x} \le \boldsymbol{u}} F_k\left(\boldsymbol{R}_c(\boldsymbol{x})\right) \tag{1}$$

The lower and upper bounds of the reduced space are then defined as [52]

$$\boldsymbol{l}^* = \min\{\boldsymbol{x}_c^{*(1)}, \ldots, \boldsymbol{x}_c^{*(N_{obj})}\} \tag{2}$$

and

$$\boldsymbol{u}^* = \max\{\boldsymbol{x}_c^{*(1)}, \ldots, \boldsymbol{x}_c^{*(N_{obj})}\} \tag{3}$$

If the misalignment between the low- and high-fidelity model is considerable, the reduced bounds may also need to take into account extreme Pareto-optimal designs obtained for the high-fidelity model [52].

The importance of the space reduction is to make construction of the data-driven model computationally feasible, particularly for higher-dimensional design spaces. It should be noted that upon reduction, the resulting fraction of the search space normally contains the entire Pareto front or its vast majority [6].

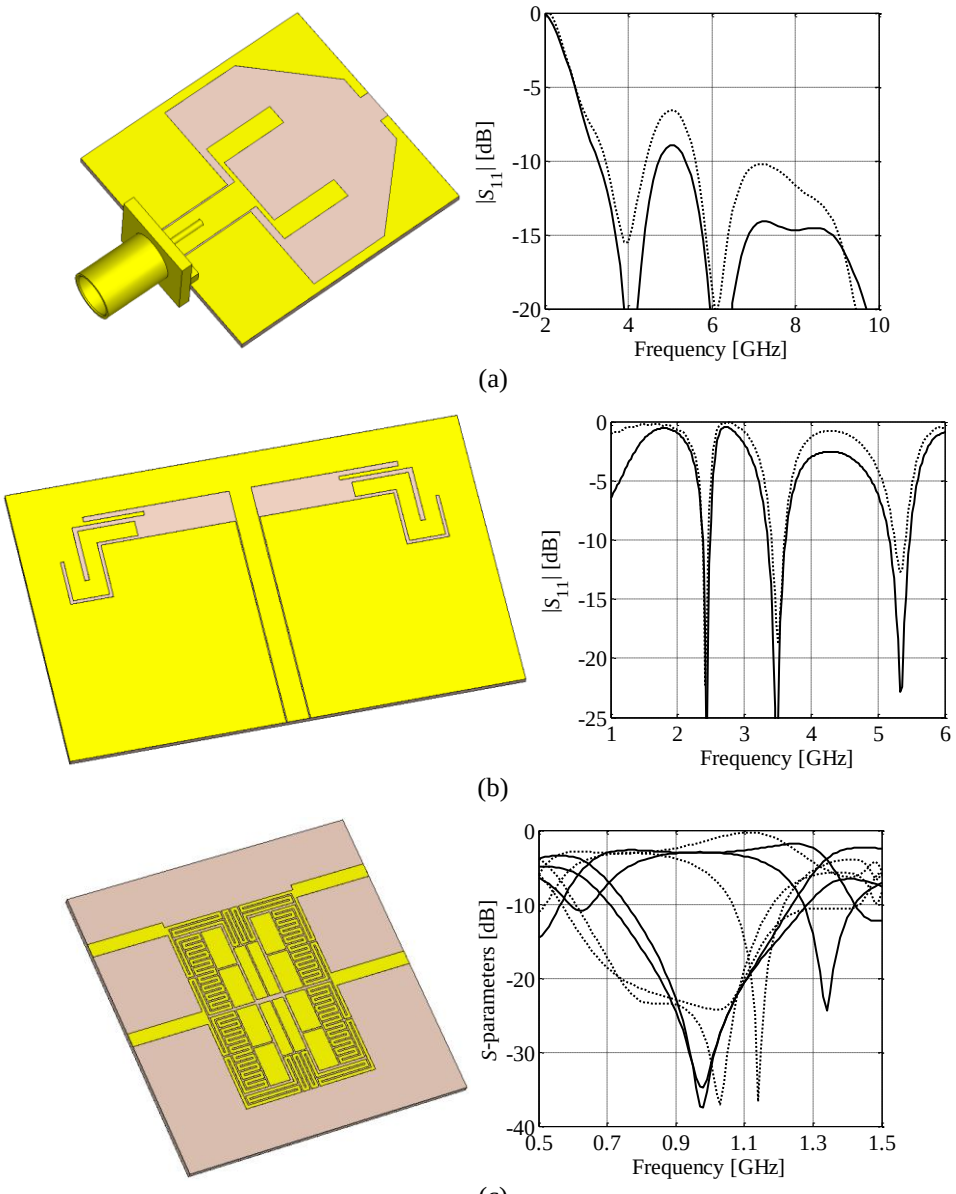

Fig. 1. Examples of antenna and microwave structures and low- (·····) and high-fidelity (—) model responses: (a) ultra-wideband monopole antenna [6] and its reflection responses, (b) miniaturized triple-band dipole antenna [56] and its reflection responses, (c) compact rat-race coupler [57]. For (a) and (b), both low- and high-fidelity models are EM simulations; for (c) the low-fidelity model is in the form of a circuit representation.

2.4. Generating Initial Pareto Set. Design Refinement

The initial approximation of the Pareto set is obtained by multi-objective optimization of the kriging surrogate model. Here, this is realized using a standard floating-point multi-objective evolutionary algorithm (MOEA) with fitness sharing, elitism mechanism, Pareto-dominance tournament selection, and mating restrictions [37]. For the sake of brevity only a short description of the algorithm is considered here. More detailed description can be found in [37], [40]. The considered MOEA is initialized using a set of designs that are evenly distributed between the extreme Pareto designs obtained using the method of Section 2.3. Upon evaluation, each design from the population is assessed based on the Pareto-dominance relation, whereas the fitness sharing mechanism is applied to prevent clustering of solutions. Selection of designs for the next iteration is based on the Pareto-ranking-based tournament selection mechanism [58]. Selection of parent individuals for crossover operation involved mating restrictions incorporated to ensure that the parents are sufficiently close to each other, which prevents the offspring to be "thrown away" from the Pareto front. The acceptable range for mating is automatically adjusted between iterations. The probabilities of mutation (implemented as random alteration of randomly selected variables of the individual with non-linear probability distribution) and arithmetic crossover are set to 0.2 and 0.5, respectively. Preservation of the best solutions is ensured using archiving and the batch-mode elitism mechanism [58].

Because the initial Pareto set is obtained through optimization of the data-driven model, it needs to be refined in order to obtain the high-fidelity-model-based Pareto designs. Let $\boldsymbol{x}_s^{(k)}$, $k = 1, \ldots, K$, be the selected elements of the Pareto front found by the

MOEA. The refinement stage exploits the output space mapping (OSM) [21] process of the following form:

$$\boldsymbol{x}_f^{(k)} \leftarrow \arg \min_{\substack{\boldsymbol{x} \\ F_2(\boldsymbol{x}) \le F_2(\boldsymbol{x}_f^{(k)}) \\ \vdots \\ F_{N_{obj}}(\boldsymbol{x}) \le F_{N_{obj}}(\boldsymbol{x}_f^{(k)})}} F_1\left(\boldsymbol{R}_s(\boldsymbol{x}) + [\boldsymbol{R}_f(\boldsymbol{x}_f^{(k)}) - \boldsymbol{R}_s(\boldsymbol{x}_f^{(k)})]\right) \quad (4)$$

The problem (4) involves minimization of F_1 and it is constrained so as not to increase the remaining objectives as compared to $\boldsymbol{x}_s^{(k)}$. The term $\boldsymbol{R}_f(\boldsymbol{x}_f^{(k)}) - \boldsymbol{R}_s(\boldsymbol{x}_f^{(k)})$ is introduced to make the corrected surrogate coincide with the high-fidelity model at the starting point (i.e., $\boldsymbol{x}_s^{(k)} = \boldsymbol{x}_s^{(k)}$). In practice, two or three iterations of (4) are sufficient to find a refined high-fidelity model design $\boldsymbol{x}_f^{(k)}$. A discrete set of high-fidelity designs is the final outcome of the optimization process. An alternative design refinement procedure based on co-kriging [59] has been described in [51].

It should be noted that acquisition of the training samples required for surrogate model construction is the major contributor to the computational cost of the considered optimization algorithm. This is because the number of points necessary to ensure acceptable accuracy of the surrogate model (say, 5% of the relative RMS error, cf. [60]) can be considerable even in the initially reduced space. From this perspective, further reduction of the computational cost is desirable. It can be achieved using segmentation-based approach which narrows down the search space to the sub-regions containing fractions of the Pareto front [54].

3. Multi-objective Optimization with Design Space Segmentation

A large number of training samples required for construction of the data-driven surrogate is a limiting factor for low-cost MOEA-based optimization. Although this

challenge can be mitigated to some extent using the initial design space reduction, data acquisition is still the main contributor to the computational cost when surrogate-based design of multi-parameter structures is considered [6]. The goal of segmentation is to further narrow down the initially reduced design space to a set of sub-regions (referred to as segments, or intervals) that enclose fractions of the Pareto front [54]. These segments are characterized by small volume, which promotes construction of accurate surrogates using a small number of data points. In this section, the segmentation approach is explained along with its novel extension that allows for maintaining equal-volume of the compartments. The section is concluded with discussion of the design framework for multi-objective optimization within the space segmentation setup.

3.1. Search Space Segmentation for Bi-Objective Problems

The formulation of the design space segmentation for bi-objective problems is as follows. Let $X_0 = \{\boldsymbol{x} : \boldsymbol{l} \leq \boldsymbol{x} \leq \boldsymbol{u}\}$ represent the region of the n-dimensional search space determined by the extreme Pareto-optimal designs $\boldsymbol{x}^{*(k)}$ (cf. Section 2.3). The volume of X_0 is defined as [54]

$$V_0 = \prod_{i = 1,\ldots,n} d_i^{(1)} \tag{5}$$

where $d_k^{(1)}$ are elements of the size vector given by

$$\boldsymbol{d}^{(1)} = [d_1^{(1)}\ d_2^{(1)}\ \ldots\ d_n^{(1)}]^T = |\boldsymbol{x}^{*(1)} - \boldsymbol{x}^{*(2)}| \tag{6}$$

The absolute value in (6) is understood as component-wise. The segmentation is realized by identifying the intermediate points located along the Pareto front between the $\boldsymbol{x}^{*(k)}$ extreme designs. The points are then used to establish a set of intervals covering the Pareto front. The combined volume of the resulting sub-domains is much smaller than the

volume of X_0. The intermediate points $\boldsymbol{x}_I^{(l)}$, l = 1, …, L, are obtained by solving a constrained single-objective problem

$$\boldsymbol{x}_I^{(l)} = \arg \min_{\boldsymbol{x},\, F_2(\boldsymbol{x}) \le F_{2.I}^{(l)}} F_1\left(\boldsymbol{R}_c(\boldsymbol{x})\right) \tag{7}$$

In general, (7) can be used to generate an arbitrary number L of auxiliary points which define L + 1 corresponding sub-domains $X_{L.p}$, p = 1, …, L + 1. The starting points for (7) are generated using $(1 - l/L)\boldsymbol{x}^{*(1)} + (l/L)\,\boldsymbol{x}^{*(2)}$ which provide a decent approximation of $\boldsymbol{x}_I^{(l)}$ under assumption that the Pareto front is non-eccentric (cf. Section 2.1). The threshold values $F_{2.I}^{(l)}$ are defined as [54]

$$F_{2.I}^{(l)} = \left(1 - \frac{l}{L}\right) F_2\left(\boldsymbol{x}^{*(1)}\right) + \frac{l}{L} F_2\left(\boldsymbol{x}^{*(2)}\right) \tag{8}$$

The volumes of the $X_{L.p}$ segments determined based on the auxiliary points are given by

$$V_{L.p} = \prod_{i=1,\ldots,n} d_{I.i}^{(l)} \tag{9}$$

where $\boldsymbol{d}_I^{(1)} = |\boldsymbol{x}^{*(1)} - \boldsymbol{x}_I^{(1)}|$, $\boldsymbol{d}_I^{(l)} = |\boldsymbol{x}_I^{(l-1)} - \boldsymbol{x}_I^{(l)}|$ for l = 2, …, L, and $\boldsymbol{d}_I^{(L+1)} = |\boldsymbol{x}^{*(2)} - \boldsymbol{x}_I^{(L)}|$. The volume of the concatenated sub-domains

$$V_L = V_{L.1} + V_{L.2} + \ldots + V_{L.L+1} \tag{10}$$

is much smaller compared to the initially reduced space X_0. In the most optimistic scenario, the volume reduction ratio is given by

$$\frac{V_L}{V_0} = \frac{1}{(L+1)^{n-1}} \tag{11}$$

In reality, however, the reduction ratios are lower than in (11) due to the lack of a mechanism that ensures equal-size compartments. Notwithstanding, segmentation substantially narrows down the search space to the region of interest and thus the combined number of training samples required for construction of local data-driven models within sub-domains is smaller compared to X_0. Conceptual illustration of the bi-

objective search space segmentation in a setup with one and two intermediate points is shown in Fig. 2.

3.2. Bi-Objective Segmentation with Equal-size Compartments

As already mentioned, there is no guarantee that the intermediate points obtained by solving (7) will result in compartments of equal size, which would lead to the best possible V_L/V_0 ratio as in (11). In case the compartment volumes are significantly different, the computational benefits of segmentation can be compromised. This problem can be mitigated by introducing geometrical constraints into (7) so as we have

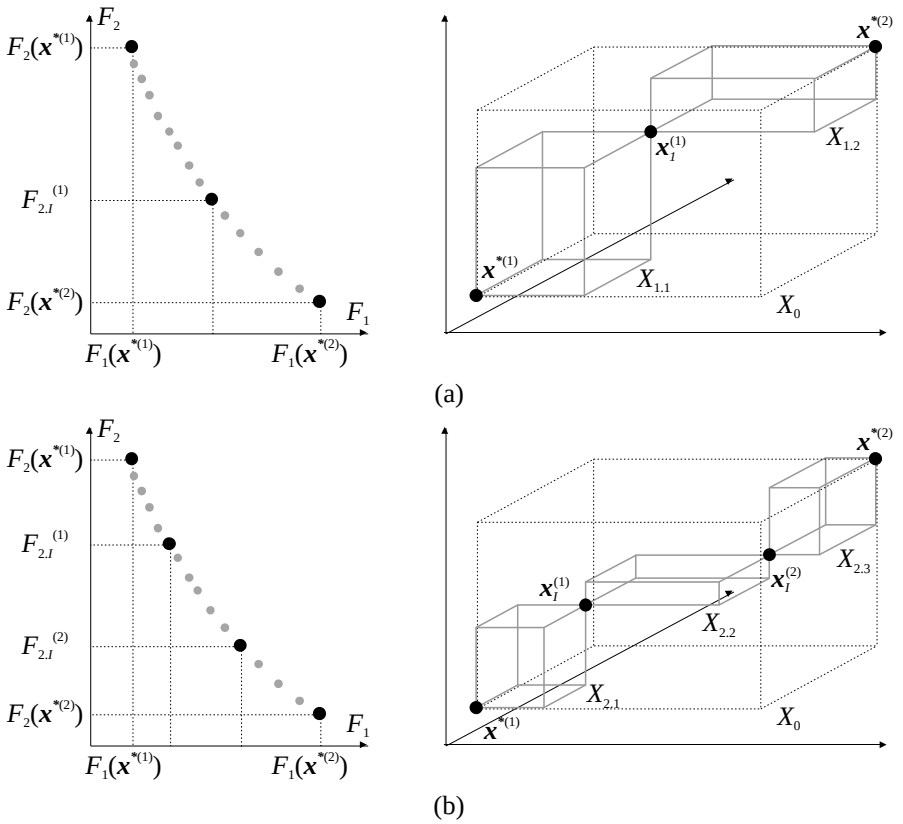

Fig. 2. Conceptual illustration of design space segmentation in bi-objective setup with: (a) one- and (b) two-intermediate points obtained by solving (7) in feature (left) and search (right) spaces. Note that L intermediate points define $L + 1$ sub-domains.

$$\boldsymbol{x}_{Ie}^{(l)} = \arg \min_{\substack{\boldsymbol{x},\, F_2(\boldsymbol{x}) \le F_{2.I}{}^{(l)} \\ V_{L.1}=V_{L.2} \\ \vdots \\ V_{L.L}=V_{L.L+1}}} F_1\left(\boldsymbol{R}_c(\boldsymbol{x})\right) \tag{12}$$

The first constraint in (12) allows for maintaining acceptable allocation of the auxiliary point in the feature space, whereas the remaining ones ensure equal-volumes of the segments. It should be noted that the solution to (12) is Pareto optimal because the volumes $V_{L.1}$, $V_{L.2}$, … $V_{L.L}$, $V_{L.L+1}$ change continuously when locations of the intermediate points along the Pareto front are adjusted. At the same time, (12) has to be solved simultaneously for all intermediate points because evaluation of the volume-related constraints requires the knowledge of all point coordinates.

3.3. Design Segmentation for Tri-Objective Problems

Conceptual illustration of the design segmentation for tri-objective problem in a two-fold segmentation setup is shown in Fig. 3. In the considered case, three auxiliary points $\boldsymbol{x}_I^{(1.2)}$, $\boldsymbol{x}_I^{(1.3)}$, $\boldsymbol{x}_I^{(2.3)}$ are required to generate four segments that cover the entire Pareto set. The points are determined by solving the following single-objective optimization problem [55]

$$\boldsymbol{x}_I^{(k.j)} = \arg \min_{\boldsymbol{x},\, F_j(\boldsymbol{x}) \le F_{j.I}{}^{(1)}} F_k\left(\boldsymbol{R}_c(\boldsymbol{x})\right) \tag{13}$$

where $k, j = 1, 2, 3$ are the indexes of the selected design objectives ($k < j$); k and j also indicate the pair of the corner points $\boldsymbol{x}^{*(k)}$ and $\boldsymbol{x}^{*(j)}$ between which the intermediate point is located (cf. Section 2.3). In (13), the optimization is performed with respect to the selected objective with constraint imposed on the second one. At the same time, the third objective is disregarded which allows for relocating the intermediate points to the "edges" of the Pareto front. Segmentation involving more intermediate points or greater number of design objectives is also possible. However, due to complexity of notation its formulation is omitted here.

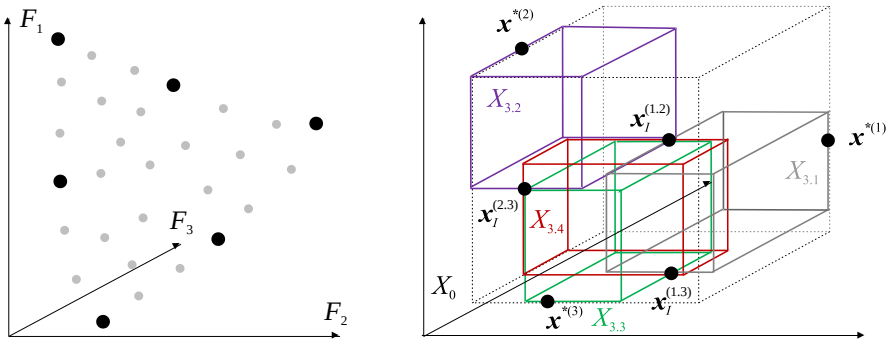

Fig. 3. Conceptual illustration of a two-fold design space segmentation in a tri-objective setup in the feature space (left) and the design space (right). The search space compartments are denoted using different colors. Note that the sub-domain $X_{3.4}$ partially overlaps with the remaining ones.

3.3. Optimization Flow

The design framework for multi-objective optimization in the segmented search space can be summarized as follows:

1. Identify extreme Pareto-optimal designs (cf. (1));
2. Perform design space reduction (cf. (2));
3. Find intermediate points and set up segmentation compartments;
4. Sample the compartments and construct the local surrogate models;
5. Find the initial Pareto set within compartments using MOEA;
6. Obtain the overall initial Pareto set by concatenating the sets found in Step 5.
7. Select designs from the overall initial Pareto set and obtain the refined set (cf. (4)).

Sampling of each sub-space and construction/updates of the surrogate model within it is performed iteratively until acceptable accuracy (verified by cross-validation [18]) is achieved. It should be emphasized that the high-fidelity model is not evaluated until the last stage of the process. Typically, around 10 to 15 refined designs are sufficient to obtain comprehensive data about available trade-offs between objectives so that the cost of the refinement process is low.

Although segmentation leads to reduction of the V_L/V_0 ratio which allows for constructing local surrogate models using limited number of training samples, identification of intermediate points required for determination of the sub-domains substantially contributes to the overall cost of the optimization process. Moreover, the number of points required for segmentation grows quickly with the number of design objectives (cf. Section 3.2). Therefore, an appropriate balance between the cost of obtaining the intermediate points (and hence their number) and computational savings resulting from the volume reduction due to space segmentation has to be sought.

4. Test Cases and Results

In this section, the segmentation-based multi-objective design framework is demonstrated using real-world engineering examples. Specifically, we perform bi-objective optimization of a miniaturized impedance transformer and a compact rat-race coupler. Comparison of the numerical results obtained using segmentation-based approach to optimization within initially reduced search space is also provided. Numerical and experimental validation of the method based on the antenna examples is considered in Sections 5 and 6.

For all of the test cases considered in this work, it is assumed that the root-mean square (RMS) error of the functional approximation models used for MOEA (setup: population size 500, algorithm duration 50 iterations) optimization is less or equal than 2.5 percent. The design of experiment approach is a modified Latin Hypercube Sampling which permits iterative addition of the samples [52], [61]. All structures are evaluated

using a dual Xeon E5540 machine with 64 GB RAM. It should be reiterated that the cost of MOEA optimization is negligible, as it is executed on a data-driven surrogate.

4.1. Wideband Impedance Transformer

The first design example is a compact impedance transformer designed to match a 50 Ohm source to a 130 Ohm load [62]. The structure is shown in Fig. 4. It is implemented on a Taconic RF-35 dielectric substrate (ε_r = 3.5, tanδ = 0.018, h = 0.762 mm) and consists of three compact microstrip resonant cells (CMRCs) arranged in a cascade connection. Its dimensions are represented using a 15-variable vector: $\boldsymbol{x}$ = [$w_{1.1}$ $w_{2.1}$ $w_{3.1}$ $l_{2.1}$ $l_{3.1}$ $w_{1.2}$ $w_{2.2}$ $w_{3.2}$ $l_{2.2}$ $l_{3.2}$ $w_{1.3}$ $w_{2.3}$ $w_{3.3}$ $l_{2.3}$ $l_{3.3}$]^T mm. Parameters w_{i1} = 1.7 mm and w_{i2} = 0.15 mm remain fixed to maintain the desired input and output impedances. The feasible region of the search space—for which consistency of the transformer topology is ensured—is defined using the following lower and upper bounds: $\boldsymbol{l}$ = [0.1 0.1 0.2 0.5 0.1 0.2 0.1 0.1 1 0.1 0.1 0.1 0.1 1 0.1]^T mm and $\boldsymbol{u}$ = [0.5 0.5 1 2 0.5 0.5 0.5 0.5 3 0.5 0.5 0.5 0.5 3 0.5]^T mm.

The high- (~1,500,000 hexahedral mesh cells, average simulation time: 8 min) and the low-fidelity (~150,000 mesh cells, simulation time: 62 s) EM models of the transformer are both implemented in CST Microwave Studio and evaluated using its time domain solver [63].

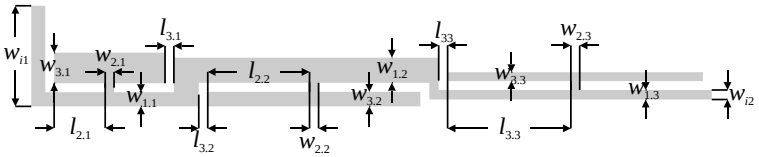

Fig. 4. Geometry of the considered 50-to-130 Ohm microstrip impedance transformer with highlight on geometric parameters [62].

Two design objectives concerning minimization of the maximum in-band reflection within 3.1 GHz to 10.6 GHz range (objective F_1) and reduction of transformer size (objective F_2) are considered. The structure size is defined as $S(\boldsymbol{x}) = A \cdot B$ where $A = (2\cdot(l_{2.1}+ l_{3.1}) + w_{2.1} + w_{1.2} + 2\cdot(l_{2.2} + l_{3.2}) + w_{2.2} + w_{1.3} + 2\cdot(l_{2.3} + l_{3.3}) + w_{2.3})$ and $B = w_{1.1}+ w_{3.1} + l_{3.1}$. It should be noted that only a part of the Pareto front for which $F_1(\boldsymbol{x}) \leq -10$ dB is considered acceptable.

The transformer has been optimized using the design framework of Section 3. The extreme Pareto-optimal designs obtained by means of single-objective optimizations w.r.t. F_1 and F_2 are $\boldsymbol{x}^{*(1)}$ = [0.4 0.17 0.91 1.66 0.14 0.45 0.13 0.19 2.31 0.16 0.15 0.17 0.15 2.34 0.14]^T mm and $\boldsymbol{x}^{*(2)}$ = [0.22 0.12 0.39 0.75 0.12 0.37 0.12 0.26 1.61 0.12 0.17 0.18 0.15 1.78 0.12]^T mm. A total cost of designs identification corresponds to 250 $\boldsymbol{R}_c$ model simulations. It should be noted that optimization for size reduction (objective F_2) has been performed with constraint imposed on maximum in-band reflection so as to ensure that it is maintained around the –10 dB threshold [6].

The intermediate design $\boldsymbol{x}_I^{(1)}$ = [0.34 0.14 0.71 1.35 0.13 0.39 0.12 0.24 1.82 0.15 0.16 0.18 0.15 1.95 0.14]^T has been found in five iterations of (7). Subsequently, the designs $\boldsymbol{x}^{*(1)}$, $\boldsymbol{x}^{*(2)}$, and $\boldsymbol{x}_{I.1}^{(1.2)}$ have been used to define sub-sections $X_{1.1}$ and $X_{1.2}$ featuring the combined volume reduction ratio of $V_1/V_0 \approx 2\cdot10^{-5}$ (cf. Fig. 2). The kriging interpolation models $\boldsymbol{R}_{s.1}$ and $\boldsymbol{R}_{s.2}$ have been constructed using 162 and 121 low-fidelity model samples, respectively. Next, both models have been optimized using MOEA and the resulting Pareto sets have been combined. Finally, a set of 10 samples—evenly allocated along F_2—has been selected and refined using (4) to the high-fidelity model level. A comparison of the high- and the low-fidelity Pareto designs obtained within the search space segments is shown in Fig. 5.

The results indicate that the selected objectives are partially conflicting. The minimum in-band reflection of –15.3 dB and maximum area of 19.5 mm^2 have been obtained for design $\boldsymbol{x}_f^{(1)}$, whereas the design $\boldsymbol{x}_f^{(10)}$ features the smallest size of 9.8 mm^2 (49.7% size reduction w.r.t. $\boldsymbol{x}_f^{(1)}$) and highest, yet still acceptable, reflection of –10.1 dB (change by 5.2 dB w.r.t. $\boldsymbol{x}_f^{(1)}$). Dimensions of the high-fidelity Pareto designs are gathered in Table 1. Frequency responses of the five selected designs are shown in Fig. 6.

The computational cost of the design process corresponds to 110 $\boldsymbol{R}_f$ model evaluations (~14.5 hours of CPU-time) and includes: 250 $\boldsymbol{R}_c$ model simulations for identification of the extreme Pareto designs, 85 $\boldsymbol{R}_c$ model evaluations for determination of the intermediate point and a total of 283 $\boldsymbol{R}_c$ model simulations required for construction the functional based approximation models within the search space segments, as well as 30 $\boldsymbol{R}_f$ model evaluations for refinement of the selected designs (three iterations per design).

For the sake of comparison, the kriging interpolation model has also been constructed within the initially reduced search space X_0. Desirable accuracy has been achieved using 502 $\boldsymbol{R}_c$ model samples. The computational cost of the design process within X_0, including $\boldsymbol{R}_s$ model identification and refinement of 10 selected samples corresponds to 127 $\boldsymbol{R}_f$ model evaluations (~17 hours of CPU time), which is 15% higher compared to optimization in a setup with two-fold segmentation. A comparison of the high-fidelity Pareto-sets obtained for both design cases is shown in Fig. 7. The obtained results are similar, with vertical discrepancies being below 1 dB which is irrelevant from practical point of view. It should be noted that the combined number of training samples required for construction of the data-driven models in $X_{1.1}$ and $X_{1.2}$ is almost two-fold lower compared to X_0. The detailed cost breakdown for both considered design cases is provided in Table 2.

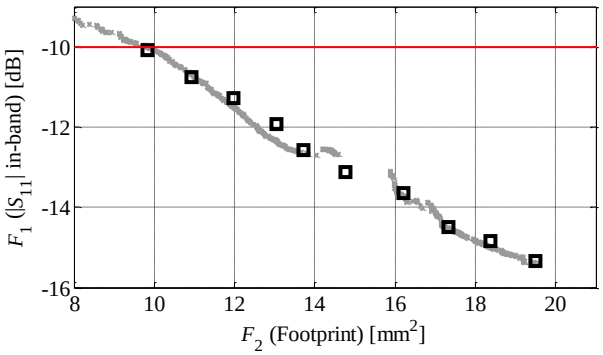

Fig. 5. The low- (×) and the high-fidelity (□) Pareto sets obtained through multi-objective optimization in a setup with two-fold segmented search space.

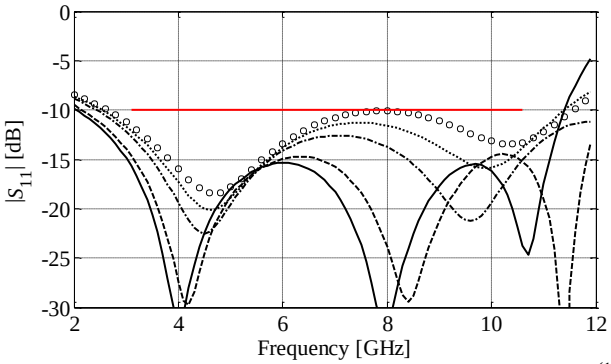

Fig. 6. Frequency characteristics of the high-fidelity Pareto optimal designs $\boldsymbol{x}_f^{(1)}$ (—),$\boldsymbol{x}_f^{(3)}$ (– –), $\boldsymbol{x}_f^{(6)}$ (–·–), $\boldsymbol{x}_f^{(8)}$ (···), and $\boldsymbol{x}_f^{(10)}$ (◦◦◦) obtained in two-fold segmented space.

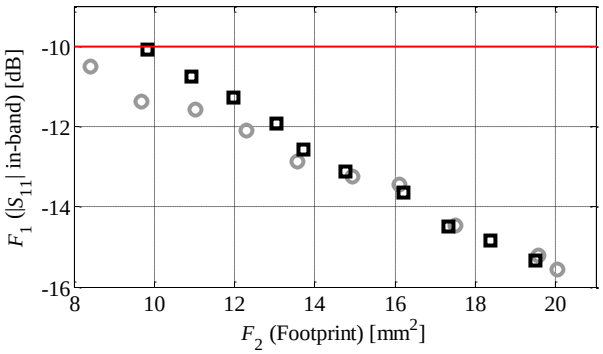

Fig. 7. A comparison of the high-fidelity Pareto sets obtained within X_0 (○) and two-fold segmented space (□).

Table 1: Compact Impedance Transformer: Structure Dimensions

		Objectives		Transformer dimensions													
		F_1 [dB]	F_2 [mm^2]	$w_{1.1}$	$w_{2.1}$	$w_{3.1}$	$l_{2.1}$	$l_{3.1}$	$w_{1.2}$	$w_{2.2}$	$w_{3.2}$	$l_{2.2}$	$l_{3.2}$	$w_{1.3}$	$w_{2.3}$	$w_{3.3}$	$l_{2.3}$	$l_{3.3}$
Designs	$\boldsymbol{x}_f^{(1)}$	–15.3	19.5	0.39	0.17	0.86	1.63	0.14	0.44	0.13	0.21	2.19	0.15	0.16	0.17	0.15	2.22	0.14
	$\boldsymbol{x}_f^{(2)}$	–14.8	18.4	0.39	0.16	0.84	1.61	0.13	0.42	0.13	0.22	2.06	0.15	0.16	0.17	0.15	2.11	0.14
	$\boldsymbol{x}_f^{(3)}$	–14.5	17.3	0.39	0.15	0.79	1.62	0.13	0.42	0.13	0.23	1.98	0.15	0.16	0.17	0.15	2.06	0.14
	$\boldsymbol{x}_f^{(4)}$	–13.6	16.2	0.37	0.14	0.75	1.56	0.13	0.43	0.13	0.22	1.95	0.16	0.16	0.17	0.15	2.03	0.14
	$\boldsymbol{x}_f^{(5)}$	–13.1	14.8	0.36	0.14	0.71	1.35	0.14	0.45	0.13	0.21	1.82	0.15	0.15	0.17	0.15	1.95	0.14
	$\boldsymbol{x}_f^{(6)}$	–12.6	13.7	0.34	0.13	0.71	1.34	0.12	0.39	0.12	0.25	1.75	0.14	0.16	0.18	0.15	1.89	0.13
	$\boldsymbol{x}_f^{(7)}$	–11.9	13.0	0.33	0.13	0.67	1.20	0.12	0.39	0.12	0.25	1.76	0.14	0.16	0.18	0.15	1.91	0.14
	$\boldsymbol{x}_f^{(8)}$	–11.3	12.0	0.33	0.13	0.61	1.05	0.12	0.39	0.12	0.25	1.76	0.14	0.16	0.18	0.15	1.91	0.13
	$\boldsymbol{x}_f^{(9)}$	–10.7	10.9	0.29	0.13	0.68	0.76	0.12	0.38	0.12	0.24	1.62	0.12	0.16	0.18	0.15	1.80	0.14
	$\boldsymbol{x}_f^{(10)}$	–10.1	9.8	0.28	0.13	0.52	0.92	0.12	0.37	0.12	0.25	1.69	0.13	0.17	0.18	0.15	1.85	0.13

Table 2. Multi-Objective Optimization of Compact Impedance Transformer: Cost Breakdown

Design steps	Search space	
	X_0	Two-fold segmentation
Auxiliary points identification	250 $\boldsymbol{R}_c$ (32.3 $\boldsymbol{R}_f$)	335 $\boldsymbol{R}_c$ (43.3 $\boldsymbol{R}_f$)
Data acquisition	502 $\boldsymbol{R}_c$ (64.8 $\boldsymbol{R}_f$)	283 $\boldsymbol{R}_c$ (36.5 $\boldsymbol{R}_f$)
MOEA optimization	N/A	N/A
Refinement	30 $\boldsymbol{R}_f$	30 $\boldsymbol{R}_f$
Total cost	127 $\boldsymbol{R}_f$ (17 h)	110 $\boldsymbol{R}_f$ (14.5 h)

4.2. Compact Rat-Race Coupler

Figure 8 shows a compact microstrip rat-race coupler (RRC) implemented on a 0.762 mm thick RF-35 substrate [35]. The structure consists of a six quarter-wavelength CMRCs with stubs and its operating frequency is 1 GHz. The vector of coupler adjustable parameters is: $\boldsymbol{x} = [w\ d_1\ d_2\ l_2\ l_{3r}\ l_{4r}\ l_{5r}]^T$. The variables $l_1 = 2d_1 + d_2 + 2.5w$, $l_3 = 0.1l_{3r}l_2$, $l_4 = 0.1l_{4r}l_3$, and $l_5 = 0.1l_{5r}l_2$ are relative to maintain consistency of the circuit in the course of the optimization process. Parameter $w_0 = 1.7$ is fixed to ensure 50 ohm port impedance. The unit for all dimensions (except the ones with r in subscript which are unit-less) is mm. The high-fidelity $\boldsymbol{R}_f$ (fine mesh, simulation time: 15 min) and the low-fidelity $\boldsymbol{R}_c$ (coarse mesh, simulation time: 220 s) models of the structure are both implemented in Sonnet ***em*** [64].

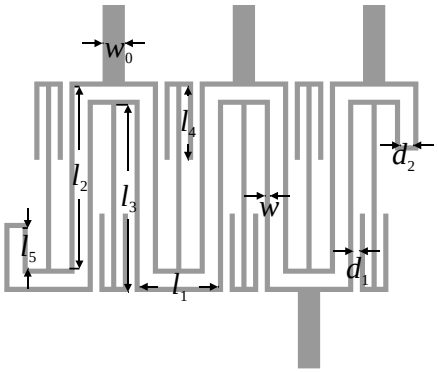

Fig. 8. Geometry of the considered compact coupler with highlighted design parameters [35].

The following design objectives are considered: F_1 – minimization of the structure size defined as $S(\boldsymbol{x}) = 35w + 24d_1 + 8d_2 + l_2$, and F_2 – maximization of the bandwidth defined for the reflection $|S_{11}|$ and isolation $|S_{41}|$ both below –20 dB. The initial lower and upper bounds of the search space are: $\boldsymbol{l} = [0.2\ 0.2\ 0.2\ 5\ 0.5\ 0.5\ 0.5]^T$ and $\boldsymbol{u} = [1.2\ 3.2\ 3.2\ 15\ 10\ 10\ 10]^T$.

The coupler structure has been optimized using segmentation-based multi-objective design framework of Section 3. The extreme Pareto designs $\boldsymbol{x}^{*(1)} = [0.2\ 0.5\ 1\ 13.3\ 10\ 9.02\ 2.59]^T$ and $\boldsymbol{x}^{*(2)} = [0.55\ 0.95\ 2.9\ 10.45\ 10\ 1.72\ 0.53]^T$, have been found using (1) after 104 and 133 evaluations of the low-fidelity model. Here, the sequential single-objective optimizations have been performed using a pattern search algorithm [65]. The segmentation setups with one and two intermediate points have been considered. For the first design case, the intermediate point $\boldsymbol{x}_I^{(1)} = [0.4\ 0.5\ 1.9\ 13.3\ 10\ 4.21\ 2.67]^T$ has been obtained after 86 $\boldsymbol{R}_c$ model evaluations (volume ratio $V_1/V_0 = 6.3\cdot10^{-2}$). For the second case, the designs $\boldsymbol{x}_I^{(1)} = [0.45\ 0.8\ 2.25\ 11.25\ 10\ 4.67\ 1.33]^T$ and $\boldsymbol{x}_I^{(2)} = [0.35\ 0.65\ 1.6\ 12.3\ 10\ 7.03\ 1.99]^T$ have been found after 83 $\boldsymbol{R}_c$ and 68 $\boldsymbol{R}_c$ model evaluations ($V_2/V_0 = 1.3\cdot10^{-3}$).

The kriging interpolation models have been constructed within the initially reduced space, as well as two- and three fold segmented spaces using 938 $\boldsymbol{R}_c$, 484 $\boldsymbol{R}_c$, and 412 $\boldsymbol{R}_c$ model samples, respectively. The low-fidelity Pareto sets obtained for each design case are shown in Fig. 9. Subsequently, ten designs have been selected from each Pareto set and refined to the high-fidelity model level. The high-fidelity Pareto designs are compared in Fig. 10. The results obtained for each design case are similar. It can be observed that the vertical differences between the designs are below 50 MHz which is considered acceptable having in mind noticeable reduction of the segmented search space

with respect to the initially reduced one. The variation of the designs along F_1 is from 921 mm^2 (265 MHz bandwidth) for the largest to 384 mm^2 (12 MHz bandwidth) for the smallest design (58% size reduction). It should be noted that the shapes of the Pareto sets are flipped along F_2 compared to the results of Section 4.1 (cf. Fig. 7), because the objective was oriented for maximization of bandwidth which has been implemented as minimization of $-F_2$ (cf. Section 2.1). The dimensions of coupler designs obtained in the two-fold segmented space are gathered in Table 3, whereas the frequency characteristics of the selected designs are shown in Fig. 11.

For the considered coupler, the computational benefits due to segmentation are 29% and 30%, for the first and second design case, respectively. A detailed cost breakdown for each considered design case can be found in Table 4. It should be noted that introduction of the intermediate points increases the computational cost due to the necessity of point identification. At the same time, the effect of narrowing the search space on reduction of the number of samples required for data-driven model construction diminishes with adding subsequent sub-domains.

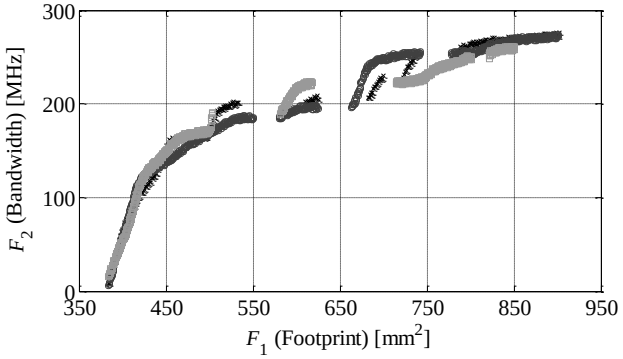

Fig. 9. Comparison of the initial Pareto-optimal sets obtained within initially reduced space (×), as well as two- (○) and three-fold (□) segmented spaces.

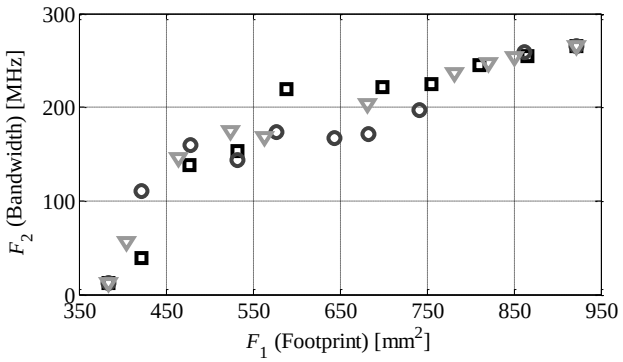

Fig. 10. Comparison of the high-fidelity Pareto-optimal sets obtained in initially reduced space (□), as well as two- (○) and three-fold (∇) segmented spaces.

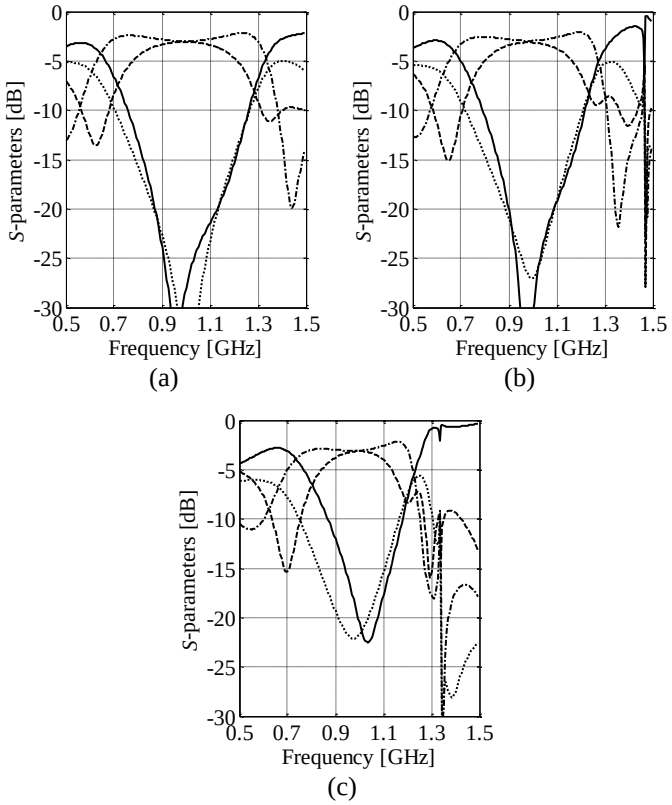

Fig. 11. Reflection (—), transmission (– –), coupling (–·–), and isolation (···) versus frequency of the selected high-fidelity Pareto designs obtained within the segmented search space with one intermediate point: (a) $\boldsymbol{x}_f^{(1)}$, (b) $\boldsymbol{x}_f^{(5)}$, and $\boldsymbol{x}_f^{(10)}$.

Table 3: Compact RRC: Dimensions of Pareto-Optimal Designs (two-fold segmentation)

		Objectives		Design parameters						
		F_1 [MHz]	F_2 [mm^2]	w	d_1	d_2	l_2	l_{3r}	l_{4r}	l_{5r}
Designs	$\boldsymbol{x}_f^{(1)}$	258.5	862	0.49	0.89	2.78	10.95	9.99	2.08	1.60
	$\boldsymbol{x}_f^{(3)}$	171.2	683	0.44	0.71	2.01	11.84	9.99	4.20	2.67
	$\boldsymbol{x}_f^{(6)}$	173.6	577	0.40	0.51	1.54	13.31	9.99	5.02	2.64
	$\boldsymbol{x}_f^{(8)}$	159.8	478	0.36	0.51	1.02	13.30	9.99	6.39	2.67
	$\boldsymbol{x}_f^{(10)}$	12.0	384	0.21	0.50	1.02	13.32	10.00	9.00	2.61

Table 4: Multi-Objective RRC Design: Cost Breakdown

Design steps	Search space		
	Initially reduced	Two-fold segmentation	Three-fold segmentation
Auxiliary points identification	237 $\boldsymbol{R}_c$ (57.9 $\boldsymbol{R}_f$)	323 $\boldsymbol{R}_c$ (79.0 $\boldsymbol{R}_f$)	388 $\boldsymbol{R}_c$ (94.8 $\boldsymbol{R}_f$)
Data acquisition	938 $\boldsymbol{R}_c$ (229.3 $\boldsymbol{R}_f$)	484 $\boldsymbol{R}_c$ (118.3 $\boldsymbol{R}_f$)	412 $\boldsymbol{R}_c$ (100.7 $\boldsymbol{R}_f$)
MOEA optimization	N/A	N/A	N/A
Refinement	20 $\boldsymbol{R}_f$	20 $\boldsymbol{R}_f$	20 $\boldsymbol{R}_f$
Total cost	307.2 $\boldsymbol{R}_f$ (76.8 h)	217.3 $\boldsymbol{R}_f$ (54.3 h)	215.6 $\boldsymbol{R}_f$ (53.8 h)

5. Scalability of Space Segmentation

Computational benefits of multi-objective optimization in a domain segmentation framework depend on the balance between the cost of obtaining auxiliary designs (intermediate points) and constructing the surrogate models. The results obtained in the previous section indicate a more or less steady growth of the cost with the number of intermediate points and limited effect of volume reduction on lowering the number of data samples required for surrogates construction. However, the coupler of Section 4.2 is characterized by a relatively small number of parameters and, hence, a relatively small volume reduction. On the other hand, it can be inferred from (11) that the combined volume of the segmented space quickly decreases with dimensionality of the problem (also see Fig. 11). Here, the effect of introducing intermediate points on the optimization cost using space segmentation is investigated based on an antenna structure with a moderate number of design parameters.

The considered antenna is an ultra-wideband (UWB) monopole implemented on a 0.762 mm RF-35 substrate (cf. Fig. 12) [66]. It comprises a trapezoidal radiator with two rectangular slots fed through a 50 Ohm microstrip line with and a ground plane with elliptical slot at the edge. The antenna is represented using a 10-variable vector: $\boldsymbol{x} = [l_0\ l_1\ w_{1r}\ w_2\ o_{2r}\ o_{3r}\ s_{1r}\ s_{2r}\ s_{4r}\ s_{5r}]^T$. The relative variables are: $w_1 = (0.5w_2 - 0.5w_0)w_{1r}$, $o_2 =$

$0.5w_2o_{2r}$, $o_3 = (l_1 - s_3)o_{3r}$, $s_1 = (0.5w_2 - 0.5w_0)s_{1r}$, $s_2 = l_1s_{2r}$, $s_4 = (w_2 - 2s_5)s_{4r}$, and $s_5 = 0.5(l_0 - g)s_{5r}$, whereas $w_0 = 1.7$, $o_1 = 0.25$, and $g = 0.5$ remain fixed. All parameters (except the unit-less ones with r in subscript) are in mm.

The considered design objectives include: F_1 – minimization of the antenna in-band reflection $|S_{11}|$ within 3.1 GHz to 10.6 GHz frequency band and F_2 – reduction of the structure size defined as $S(\boldsymbol{x}) = w_2(l_0 + l_1)$. Consistency of the structure geometry is maintained for the initial lower/upper bounds: $\boldsymbol{l}_0 = [4\ 3\ 0\ 4\ 0\ 0\ 0.1\ 0\ 0.01\ 0.01]^T$ and $\boldsymbol{u}_0 = [24\ 24\ 1\ 24\ 0.5\ 1\ 0.9\ 0.3\ 0.5\ 0.5]^T$. The low- (1,500,000 cells, simulation time: 330 s) and high-fidelity (6,000,000 cells, simulation time: 30 min) models of the structure are implemented in CST Studio [63]. To ensure reliability of the simulation results both antenna models incorporate the SubMiniature version A (SMA) connectors.

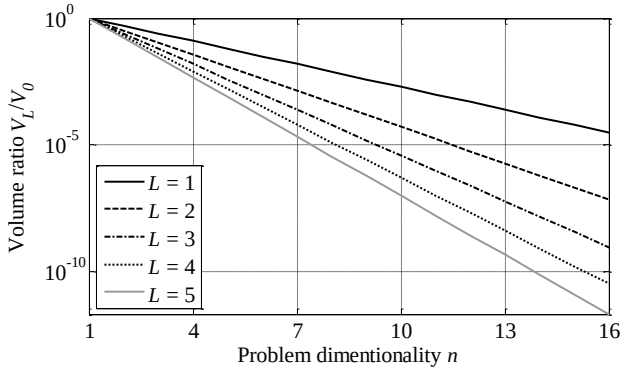

Fig. 11. Change of the volume ratio (11) as a function of problem dimensionality for the design space defined using one ($L = 1$) to five ($L = 5$) segments. The reduction radio becomes less pronounced with increase of the number of segments.

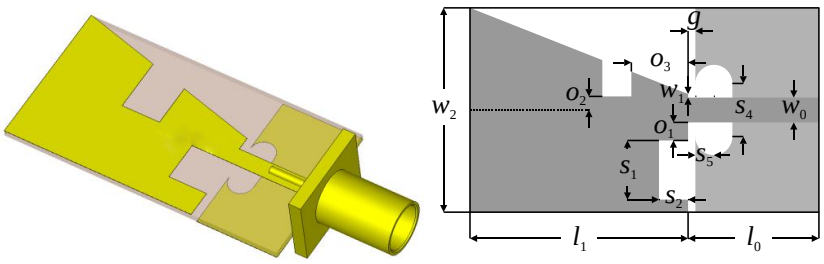

(a) (b)

Fig. 12. Trapezoidal-shape UWB monopole antenna: (a) visualization of the structure with the SMA connector and (b) geometry with marked design parameters [66].

The effect of design space segmentation on the computational cost of the antenna optimization is investigated for X_0, as well as for a setup with one to four intermediate points. Here, single-objective optimizations are performed using a numerically efficient gradient-based algorithm embedded in a trust-region (TR) framework [67]. The extreme Pareto designs $\boldsymbol{x}^{*(1)}$ = [9.31 15.62 0.37 14.81 0.06 0.08 0.68 0.12 0.13 0.29]^T (optimal w.r.t. F_1) and $\boldsymbol{x}^{*(2)}$ = [9.13 13.11 0.26 12.38 0 0.12 0.74 0.19 0.05 0.43]^T (optimal w.r.t. F_2) have been found after 85 $\boldsymbol{R}_c$ and 107 $\boldsymbol{R}_c$ model evaluations, respectively. Subsequently, the TR-based algorithm has been used to identify intermediate points for the two- to five-fold segmented spaces. The volume reduction ratios for each case are $V_1/V_0 = 1.6\cdot10^{-3}$, $V_2/V_0 = 3.9\cdot10^{-5}$, $V_3/V_0 = 3.8\cdot10^{-6}$, $V_4/V_0 = 4.7\cdot10^{-7}$, respectively. Next, the kriging surrogates have been constructed within the initially reduced and segmented spaces using 1352 $\boldsymbol{R}_c$, 514 $\boldsymbol{R}_c$, 206 $\boldsymbol{R}_c$, 208 $\boldsymbol{R}_c$, and 230 $\boldsymbol{R}_c$ model samples and optimized using MOEA. Figure 13 shows comparison of the obtained low-fidelity Pareto sets. Finally, ten designs have been selected from the initial Pareto sets and refined. The obtained Pareto sets given in Fig. 14 are close to each other. Their vertical discrepancies are below 1 dB which is practically negligible. The Pareto sets range along F_2 from around 281 mm^2 (close to –10 dB in-band reflection) to 369 mm^2 (around –12 dB reflection). The smallest design features around 24% size reduction compared to the largest one. The detailed cost breakdown of the design process in considered setups is shown in Table 5.

Table 5: Segmentation Scalability: Cost Breakdown

Design steps	Search space				
	L = 0 (X_0)	L = 1 two segments	L = 2 three segments	L = 3 four segments	L = 4 five segments
Auxiliary points identification	192 $\boldsymbol{R}_c$ (35.2 $\boldsymbol{R}_f$)	264 $\boldsymbol{R}_c$ (48.4 $\boldsymbol{R}_f$)	345 $\boldsymbol{R}_c$ (63.3 $\boldsymbol{R}_f$)	376 $\boldsymbol{R}_c$ (68.9 $\boldsymbol{R}_f$)	457 $\boldsymbol{R}_c$ (83.8 $\boldsymbol{R}_f$)
Data acquisition	1352 $\boldsymbol{R}_c$ (247.9 $\boldsymbol{R}_f$)	514 $\boldsymbol{R}_c$ (94.2 $\boldsymbol{R}_f$)	206 $\boldsymbol{R}_c$ (37.8 $\boldsymbol{R}_f$)	208 $\boldsymbol{R}_c$ (38.1 $\boldsymbol{R}_f$)	230 $\boldsymbol{R}_c$ (42.2 $\boldsymbol{R}_f$)
MOEA optimization	N/A	N/A	N/A	N/A	N/A
Refinement	30 $\boldsymbol{R}_f$	30 $\boldsymbol{R}_f$	30 $\boldsymbol{R}_f$	30 $\boldsymbol{R}_f$	30 $\boldsymbol{R}_f$
Total cost	313.1 $\boldsymbol{R}_f$ (156.5 h)	172.6 $\boldsymbol{R}_f$ (86.3 h)	131.0 $\boldsymbol{R}_f$ (65.5 h)	137.1 $\boldsymbol{R}_f$ (68.5 h)	156.0 $\boldsymbol{R}_f$ (78.0 h)

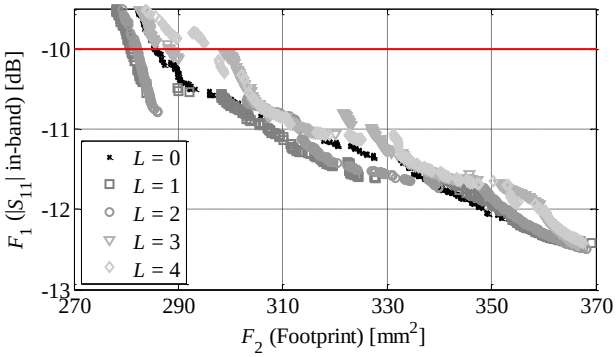

Fig. 13. Scalability of design segmentation: comparison of the low-fidelity Pareto sets obtained within the search spaces with zero (L = 0) to four (L = 5) intermediate points (one to five segments). Note that vertical discrepancies between the sets are below 1 dB which is practically negligible.

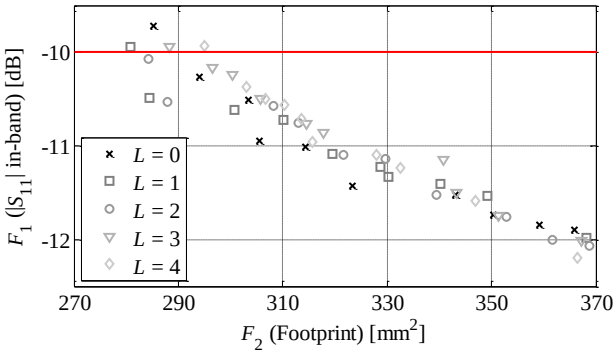

Fig. 14. Scalability of design segmentation: high-fidelity Pareto sets obtained in search spaces with one to five segments.

The effect of segmentation setup on multi-objective design cost (normalized to the number of $\boldsymbol{R}_f$ model simulations) is shown in Figure 15. The simulation results indicate that the cost of single-objective optimizations increases in close-to-linear fashion with the number of intermediate points. At the same time, the number of training samples required for construction of the functional approximation surrogate decreases rapidly for setups with two and three search space compartments. However, further increase of the number of intermediate points does not lead to a reduction of the cost kriging model construction. Based on the results obtained for the considered antenna, 30 $\boldsymbol{R}_c$ to 40 $\boldsymbol{R}_c$ model samples are required to maintain acceptable accuracy of the surrogate. Another important observation is

that for $L > 1$, identification of the intermediate points becomes the main contributor to the overall cost of the design process. As shown in Table 4, where single-objective optimizations have been performed using pattern search, the design cost savings due to increasing the number of segments from two to three are the order of only a few $\boldsymbol{R}_f$ simulations. Here, however, the difference in optimization cost between two- and three-fold segments is a few dozen of $\boldsymbol{R}_f$ evaluations (cf. Table 5). Based on that, one can conclude that segmentation in a setup with more than one auxiliary point is not practical unless efficient single-objective algorithms are used.

6. Selected Topics

In this section, application of space segmentation for multi-objective design of a planar antenna structure is investigated. Specifically, the structure is optimized using the methodology proposed in Section 3.2 that allows for maintaining equal-size of the design space compartments. Furthermore, optimization of the antenna in tri-objective setup and experimental validation of the designs are considered.

6.1. Antenna Structure

The last considered structure is an ultra-wideband antenna shown in Fig. 16 [68]. It comprises a rectangular monopole radiator with two symmetrical slots. The antenna is fed through a 50 Ohm microstrip line with ground plane modification in the form of an elliptical slit below the feed line. It is implemented on a 1.55 mm thick FR4 dielectric substrate ($\varepsilon_r = 4.3$, $\tan\delta = 0.025$). The antenna parameters are $\boldsymbol{x} = [l_g\ l_0\ l_1\ w_1\ w_2\ o_1\ l_2\ w_3\ o_2\ s_1\ s_2]^T$, whereas the dimension $w_0 = 2.0$ is fixed (all parameters are in mm). The EM antenna models are both implemented in CST Studio ($\boldsymbol{R}_f$: ~2,200,000 mesh cells,

simulation time 15 minutes, and $\boldsymbol{R}_c$: ~160,000 cells, 40 seconds) along with SMA connectors (required for reliability of the simulation results). The design space is defined by the lower and upper bounds: $\boldsymbol{l}$ = [2 2 2 0.2 2 0 0.1 0.1 0 0.01 0.01]^T mm and $\boldsymbol{u}$ = [15 15 20 3 15 15 3 8 5 0.8 0.8]^T mm.

6.2. Segmentation with Equal-Volume Segments

Two design objectives considered: F_1 – minimization of reflection $S(\boldsymbol{x})$ = max{$|S_{11}|_{\text{from 3.1 GHz to 10.6 GHz}}$}, and F_2 – reduction of antenna size $A(\boldsymbol{x}) = (2o_2 + 2w_3 + 2w_1 + w_2)(l_0 + 2l_2 + l_1 + o_1)$. It should be reiterated that only the designs for which the in-band reflection is below the –10 dB threshold are of interest.

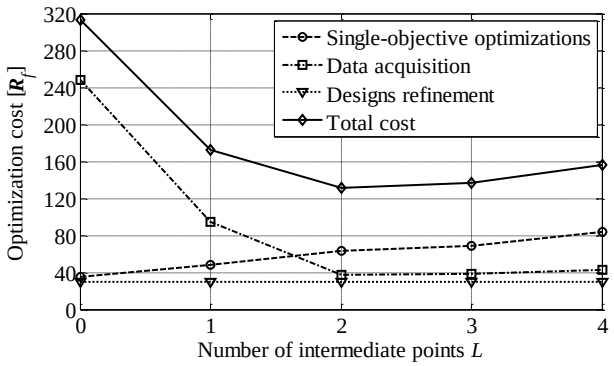

Fig. 15. Scalability of design space segmentation: the effect of algorithm setup in terms of the number of segments on computational cost of multi-objective optimization.

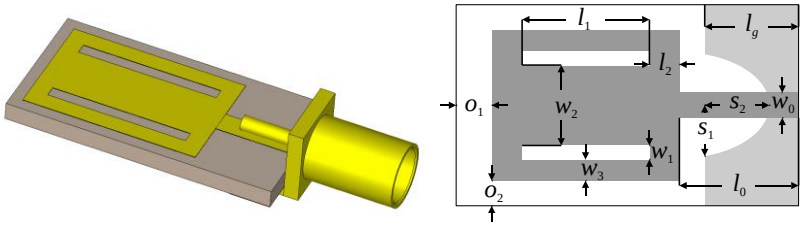

(a) (b)

Fig. 16. Planar UWB antenna: (a) visualization of the structure with an SMA connector, and (b) antenna geometry with highlighted design parameters [68].

The extreme Pareto designs $\boldsymbol{x}^{*(1)}$ = [8.86 12.96 9.39 0.35 3.88 6.46 1.21 1.58 2.58 0.33 0.54]^T (optimal w.r.t. F_1) and $\boldsymbol{x}^{*(2)}$ = [9.26 13.19 8.9 0.24 3.28 0 0.69 1.45 0.71 0.66 0.61]^T (optimal w.r.t. F_2) have been obtained after 107 $\boldsymbol{R}_c$ and 156 $\boldsymbol{R}_c$ simulations, respectively. The intermediate point for equal-volume two-fold segmentation $\boldsymbol{x}_{Ie}^{(1)}$ = [9.02 12.96 9.08 0.29 3.74 2.56 0.75 1.45 1.32 0.52 0.55]^T has been obtained after 7 iterations of (12). For the sake of comparison, the intermediate point $\boldsymbol{x}_I^{(1)}$ = [9.05 13 9.02 0.22 3.51 3.06 0.83 1.44 1.57 0.51 0.58]^T has been also obtained using (7). Subsequently, the kriging interpolation models have been constructed within the compartments featuring equal and unequal volumes and the initially reduced space using 184 $\boldsymbol{R}_c$, 264 $\boldsymbol{R}_c$, and 702 $\boldsymbol{R}_c$ samples, respectively. Finally, the selected low-fidelity Pareto designs have been refined. A comparison of the low- and high-fidelity Pareto sets obtained for each design case is shown in Fig. 17. The discrepancies between the resulting Pareto sets along F_1 are below 1 dB, which makes them practically irrelevant. The variation of the Pareto designs along the Pareto front is from –13.6 dB (390 mm^2) to –9.9 dB (193 mm^2). The size reduction of the smallest antenna design with respect to the largest one is 50.5%. The frequency characteristics of the selected Pareto optimal designs obtained within two-fold segmented space with equal-size compartments are shown in Fig. 18, whereas their corresponding dimensions are gathered in Table 6.

A detailed cost breakdown for the considered design cases is given in Table 7. The obtained results indicate that the cost of data acquisition within the compartments obtained from (12) is 30% lower than for the ones determined using (7). Consequently, application of segmentation in a setup with equal-volume compartments can be useful for reducing the overall cost of multi-objective optimization. It is also expected that the

computational savings due to using (12) will be more pronounced when simulation time ratio between the $\boldsymbol{R}_c$ and $\boldsymbol{R}_f$ is lower than in the considered case.

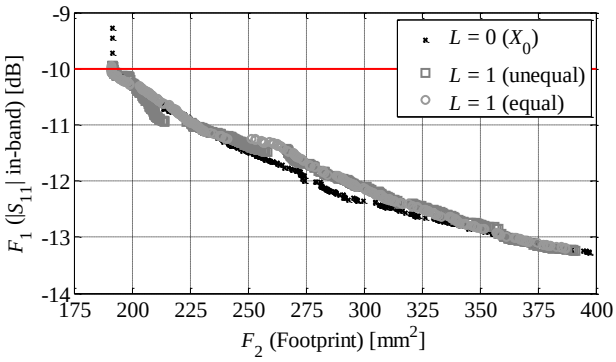

(a)

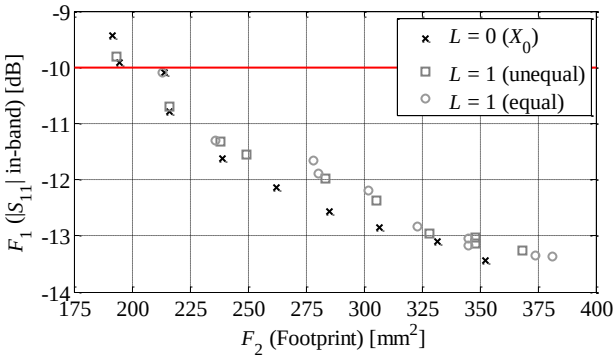

(b)

Fig. 17. Comparison of Pareto designs obtained within the initially reduced and two-fold segmented spaces with equal- and unequal-size compartments: (a) low- and (b) high-fidelity designs.

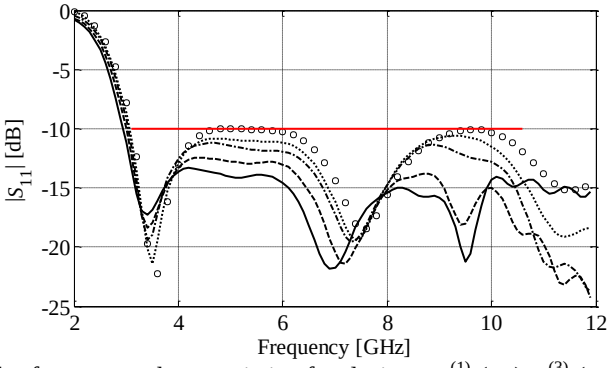

Fig. 18. UWB monopole: frequency characteristics for designs $\boldsymbol{x}_f^{(1)}$ (—),$\boldsymbol{x}_f^{(3)}$ (– –), $\boldsymbol{x}_f^{(5)}$ (–·–), $\boldsymbol{x}_f^{(7)}$ (···), and $\boldsymbol{x}_f^{(9)}$ (◦◦◦) obtained within two-fold segmented space with equal-size compartments.

Table 6: UWB antenna: Dimensions of Pareto- Designs Obtained in Two-Fold Segmented Space with Equal-Size Compartments

	Objectives		Design parameters										
	F_1 [dB]	F_2 [mm^2]	l_g	l_0	l_1	w_1	w_2	o_1	l_2	w_3	o_2	s_1	s_2
Designs $\boldsymbol{x}_f^{(1)}$	–13.3	372	8.97	12.98	9.22	0.30	3.76	5.15	1.10	1.56	2.55	0.34	0.55
$\boldsymbol{x}_f^{(3)}$	–12.3	294	9.14	13.03	9.13	0.29	3.63	3.04	0.87	1.53	1.83	0.45	0.56
$\boldsymbol{x}_f^{(5)}$	–11.2	236	9.24	13.14	8.94	0.27	3.46	1.42	0.77	1.46	1.24	0.56	0.61
$\boldsymbol{x}_f^{(7)}$	–10.6	215	9.25	13.12	9.04	0.25	3.29	0.07	0.82	1.46	1.15	0.58	0.61
$\boldsymbol{x}_f^{(9)}$	–9.9	193	9.25	13.08	8.90	0.25	3.29	0.00	0.70	1.48	0.76	0.64	0.61

Table 7: UWB Monopole: Cost Breakdown in a Setup With and Without Equal-Size Segments

Design steps	Search space		
	L = 0 (X_0)	L = 1 unequal-size	L = 1 equal-size
Auxiliary points identification	263 $\boldsymbol{R}_c$ (11.7 $\boldsymbol{R}_f$)	348 $\boldsymbol{R}_c$ (15.5 $\boldsymbol{R}_f$)	354 $\boldsymbol{R}_c$ (15.7 $\boldsymbol{R}_f$)
Data acquisition	702 $\boldsymbol{R}_c$ (31.2 $\boldsymbol{R}_f$)	264 $\boldsymbol{R}_c$ (11.7 $\boldsymbol{R}_f$)	184 $\boldsymbol{R}_c$ (8.2 $\boldsymbol{R}_f$)
MOEA optimization	N/A	N/A	N/A
Refinement	30 $\boldsymbol{R}_f$	30 $\boldsymbol{R}_f$	30 $\boldsymbol{R}_f$
Total cost	72.9 $\boldsymbol{R}_f$ (18.2 h)	57.2 $\boldsymbol{R}_f$ (14.3 h)	53.9 $\boldsymbol{R}_f$ (13.5 h)

6.3. Tri-Objective Optimization

In the last case study, optimization of the UWB antenna using design segmentation framework in a setup with three requirements is considered (cf. Section 3.3) [55]. The first two design objectives considered here are the same as the example of Section 6.2, whereas the third one, denoted as F_3, is oriented for minimization of realized gain variability within 3.1 GHz to 10.6 GHz band. The first two extreme Pareto-optimal designs obtained through minimization of (1) are the same as in Section 6.2. The third one: $\boldsymbol{x}^{*(3)}$ = [8.38 12.82 9.89 0.65 3.84 14.99 1.54 1.68 2.65 0.39 0.55]^T has been obtained for explicit optimization with respect to objective F_3 while maintaining in-band reflection below the acceptable –10 dB threshold.

The intermediate points $\boldsymbol{x}_I^{(1.2)}$ = [9.12 13.04 8.79 0.29 3.43 2.91 0.87 1.38 1.48 0.53 0.57]^T, $\boldsymbol{x}_I^{(1.3)}$ = [8.72 12.8 9.53 0.51 3.95 11.36 1.33 1.61 2.5 0.35 0.54]^T, and $\boldsymbol{x}_I^{(2.3)}$ = [8.8

12.99 9.42 0.45 3.59 7.25 1.1 1.57 1.6 0.54 0.57]^T have been obtained from (13) and used for construction of the segmented search space ($V_4/V_0 \approx 10^2$). The kriging surrogates have been then identified in the segmented space and optimized using the algorithm of Section 2.4. Finally, fifteen low-fidelity designs selected from the concatenated initial Pareto set have been refined. Dimensions of ten selected high-fidelity designs are given in Table 8, whereas the frequency responses of five of them are shown in Fig. 19. The obtained results indicate inverse relation between the antenna size (objective F_2) and the in-band antenna gain variability (objective F_3). Consequently, among the designs from Table 8, large antenna (496 mm^2) with moderate reflection (–11 dB) features the smallest gain variability of 3 dB. Note that increasing antenna size permits improved impedance matching (objective F_1). The minimum value of –13.7 dB has been obtained for the structures characterized by footprints of 428 mm^2 (gain variability of 4.3 dB) and 446 mm^2 (gain variability 4.1), respectively. Consequently, for the considered structure, there is evident trade-off between the size and other performance figures.

The high-fidelity Pareto-optimal optimal designs $\boldsymbol{x}_f^{(1)}$, $\boldsymbol{x}_f^{(5)}$ and $\boldsymbol{x}_f^{(9)}$ (cf. Table 8) have been fabricated and measured. The photographs of manufactured antennas is shown in Fig. 20, whereas their performance characteristics are compared in Figs. 21 and 22. The obtained results are in good agreement. The discrepancies between the simulations and measurements are mostly due to fabrication and assembly tolerances, as well as electrically large measurement setup which was not accounted for in the EM simulation models. Radiation patterns of the antenna obtained in H- and E-planes are shown in Figs. 23 and 24. It should be noted that besides deterioration of the E-plane patterns resulting from connector shielding during the measurements, the characteristics are in good agreement.

Optimization of the antenna has been also performed within X_0. A comparison of the initial Pareto sets obtained in the initially reduced and segmented spaces is shown in Fig. 25, whereas a detailed cost breakdown for both cases is provided in Table 9. The obtained results indicate that two-fold segmentation allows for reducing the number of samples required for accurate representation of the design space by over 55% compared to X_0. On the other hand, the cost of obtaining the intermediate points increased by over 35% and thus the cost reduction due to two-fold segmentation (excluding the refinement step) is around 20%. It should be noted that three-fold segmentation would involve identification of three more intermediate points (six designs in total) which is numerically impractical for the considered design problem.

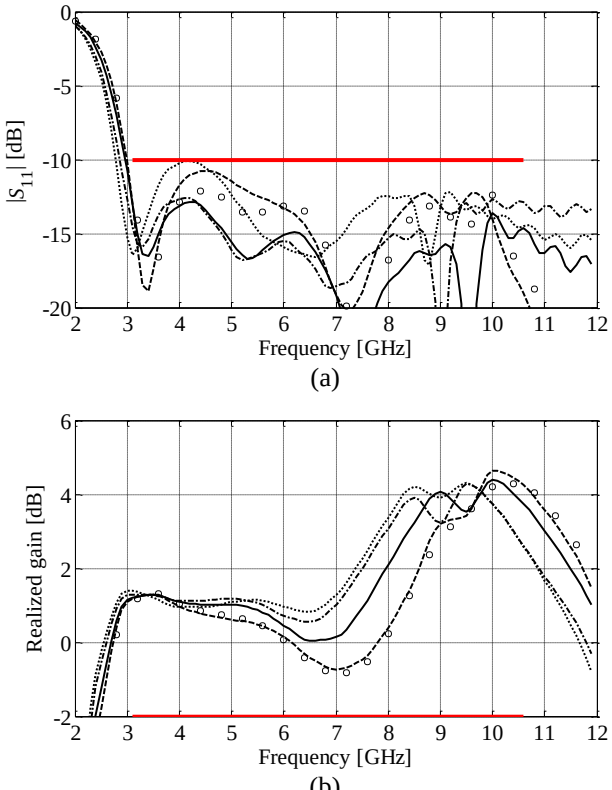

Fig. 19. Frequency results for high-fidelity designs $\boldsymbol{x}_f^{(1)}$ (—),$\boldsymbol{x}_f^{(3)}$ (– –), $\boldsymbol{x}_f^{(5)}$ (–·–), $\boldsymbol{x}_f^{(7)}$ (···), and $\boldsymbol{x}_f^{(9)}$ (◦◦◦) of the UWB monopole optimized in three-objective setup with search space segmentation: (a) reflection and (b) gain.

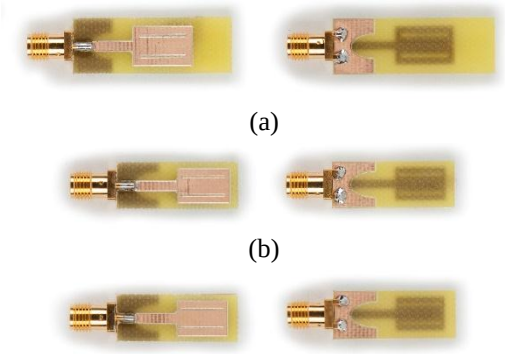

(a)

(b)

(c)

Fig. 20. Photographs (in-scale) of the selected high-fidelity Pareto designs of UWB antenna optimized in three-objective setup with domain segmentation: (a) $\boldsymbol{x}_f^{(1)}$, (b) $\boldsymbol{x}_f^{(5)}$, and (c) $\boldsymbol{x}_f^{(9)}$.

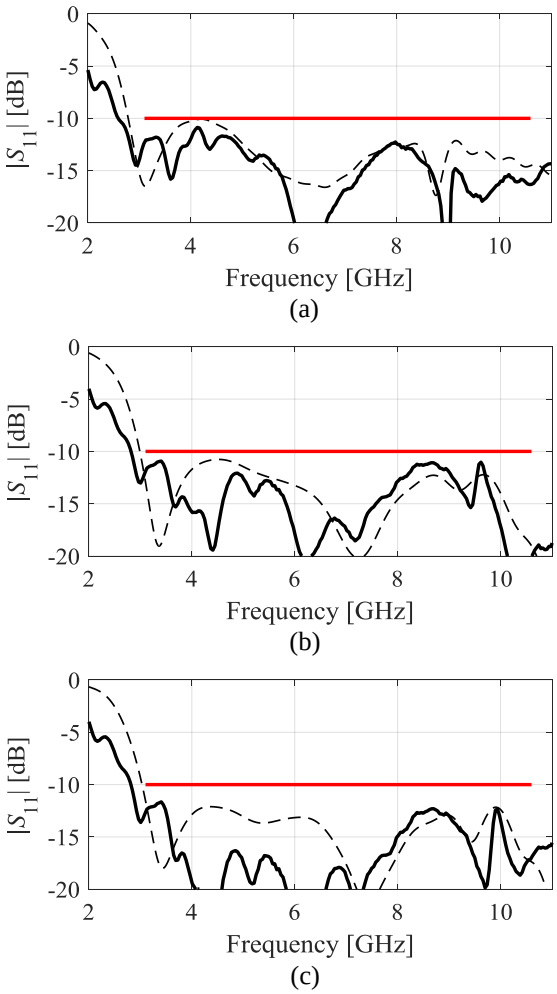

(a)

(b)

(c)

Fig. 21. Comparison of simulated (– –) and measured (—) reflection characteristics obtained for Pareto-optimal designs: (a) $\boldsymbol{x}_f^{(1)}$, (b) $\boldsymbol{x}_f^{(5)}$, and (c) $\boldsymbol{x}_f^{(9)}$.

Table 8: Tri-Objective Antenna Design: Pareto Set Obtained in Two-Fold Segmented Search Space

		Objectives			Design parameters										
		F_1 [dB]	F_2 [mm^2]	F_3 [dB]	l_g	l_0	l_1	w_1	w_2	o_1	l_2	w_3	o_2	s_1	s_2
Designs	$\boldsymbol{x}_f^{(1)}$	–10.1	400	3.5	8.60	12.81	9.86	0.57	3.85	8.44	1.34	1.63	1.80	0.44	0.56
	$\boldsymbol{x}_f^{(2)}$	–13.7	428	4.3	9.00	12.92	9.22	0.43	3.71	9.31	1.09	1.56	2.51	0.35	0.55
	$\boldsymbol{x}_f^{(3)}$	–12.6	476	3.7	8.77	12.85	9.53	0.58	3.83	11.61	1.14	1.64	2.43	0.36	0.56
	$\boldsymbol{x}_f^{(4)}$	–11.0	298	4.8	8.90	12.88	9.15	0.44	3.62	2.91	1.29	1.6	1.57	0.44	0.56
	$\boldsymbol{x}_f^{(5)}$	–10.8	253	5.4	9.14	13.07	9.26	0.36	3.50	1.86	0.79	1.46	1.33	0.55	0.59
	$\boldsymbol{x}_f^{(6)}$	–12.9	497	3.6	8.80	12.84	9.47	0.52	3.88	12.67	1.10	1.64	2.58	0.35	0.56
	$\boldsymbol{x}_f^{(7)}$	–12.9	380	4.4	8.93	12.83	8.92	0.50	3.84	7.93	0.95	1.56	2.03	0.44	0.55
	$\boldsymbol{x}_f^{(8)}$	–11.0	496	3.0	8.57	12.88	9.64	0.61	3.89	13.76	1.38	1.64	2.16	0.37	0.56
	$\boldsymbol{x}_f^{(9)}$	–11.5	261	5.1	9.19	13.02	8.99	0.39	3.53	2.30	0.72	1.49	1.42	0.53	0.60
	$\boldsymbol{x}_f^{(10)}$	–13.7	446	4.1	9.07	12.94	9.15	0.51	3.75	11.25	1.08	1.52	2.38	0.38	0.55

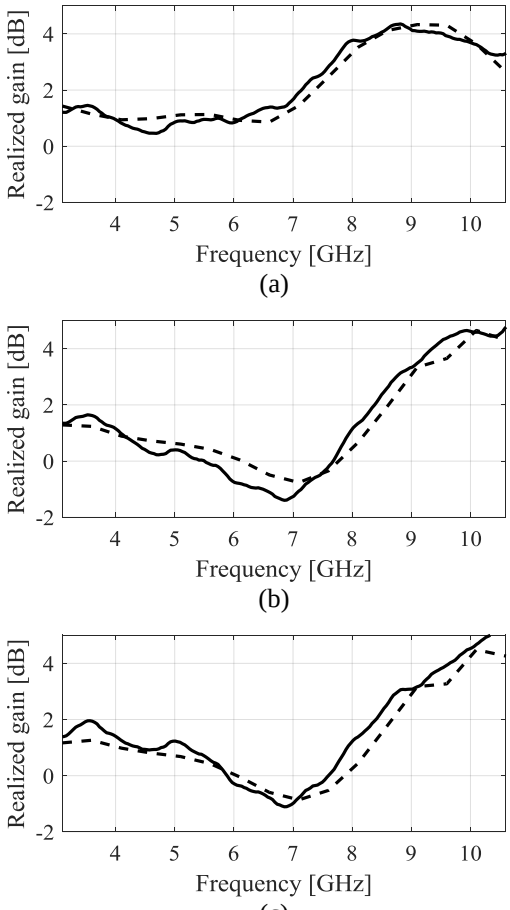

Fig. 22. Comparison of simulated (– –) and measured (—) gain characteristics obtained for Pareto-optimal designs: (a) $\boldsymbol{x}_f^{(1)}$, (b) $\boldsymbol{x}_f^{(5)}$, and (c) $\boldsymbol{x}_f^{(9)}$.

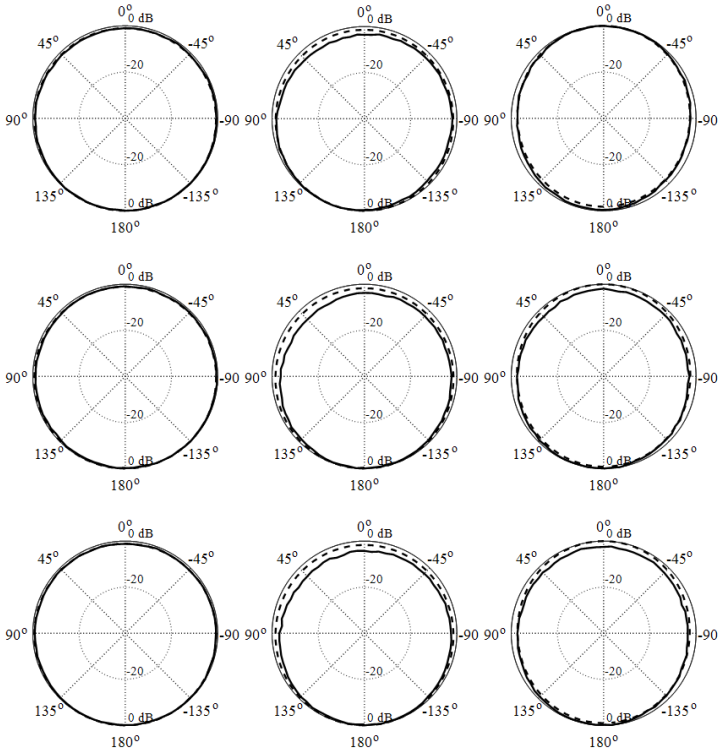

(a) (b) (c)

Fig. 23. Comparison of simulated (– –) and measured (—) H-plane radiation patterns obtained for the design $\boldsymbol{x}_f^{(1)}$ (top), $\boldsymbol{x}_f^{(5)}$ (middle), and $\boldsymbol{x}_f^{(9)}$ (bottom) at: (a) 4 GHz, (b) 6 GHz, and (c) 8 GHz frequency.

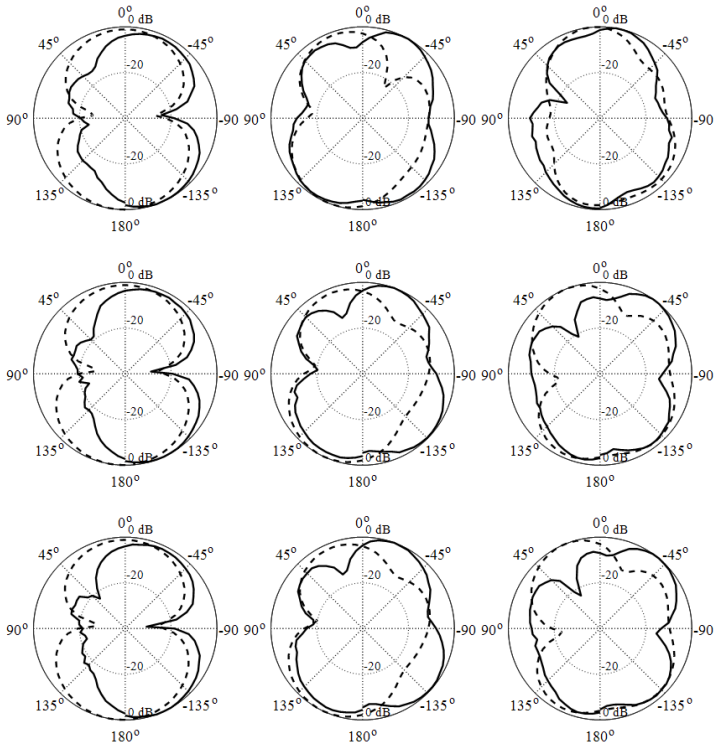

(a) (b) (c)

Fig. 23. Comparison of simulated (– –) and measured (—) E-plane radiation patterns obtained for the design $\boldsymbol{x}_f^{(1)}$ (top), $\boldsymbol{x}_f^{(5)}$ (middle), and $\boldsymbol{x}_f^{(9)}$ (bottom) at: (a) 4 GHz, (b) 6 GHz, and (c) 8 GHz frequency.

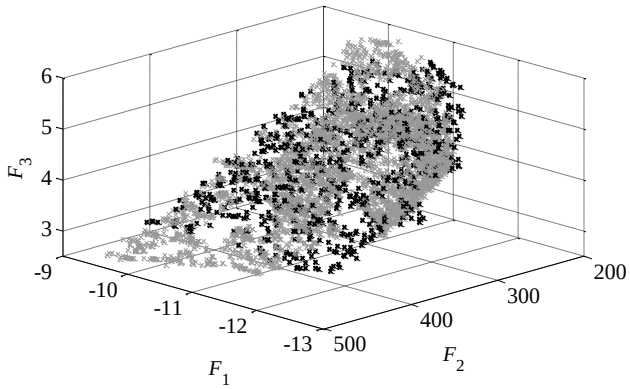

Fig. 25. Comparison of the initial Pareto sets obtained within X_0 (gray) and two-fold segmented search space (black).

Table 9: Tri-objective Optimization of UWB Monopole: Cost Breakdown

Design steps	Search space	
	X_0	Two-fold segmentation
Auxiliary points identification	347 $\boldsymbol{R}_c$ (15.4 $\boldsymbol{R}_f$)	569 $\boldsymbol{R}_c$ (25.3 $\boldsymbol{R}_f$)
Data acquisition	843 $\boldsymbol{R}_c$ (37.5 $\boldsymbol{R}_f$)	372 $\boldsymbol{R}_c$ (16.5 $\boldsymbol{R}_f$)
MOEA optimization	N/A	N/A
Refinement	45 $\boldsymbol{R}_f$	45 $\boldsymbol{R}_f$
Total cost	97.9 $\boldsymbol{R}_f$ (24.5 h)	86.8 $\boldsymbol{R}_f$ (21.7 h)

7. Conclusion

A framework for expedited multi-objective optimization of expensive computational models has been discussed. The framework exploits variable-fidelity simulations, data-driven surrogates, and initial design space reduction. One of the main challenges related to utilization of the approach to design of multi-parameter structures is high cost of acquiring the training data necessary to construct the approximation surrogates. In this work, the problem has been addressed by means of space segmentation. The technique aims at reducing the volume of the search space portion that needs to be sampled while maintaining the coverage of the Pareto front. The latter is encapsulated within a set of intervals (or compartments) defined by auxiliary

intermediate points obtained through supplementary single-objective optimization runs. The combined volume of the obtained segments is significantly smaller than the volume of the initially reduced space which allows for constructing accurate data-driven surrogates using limited number of samples. The segmentation methodology has been described in details and further extended using a novel mechanism that promotes division of the search space into equal-volume compartments. It has been validated using several real-world design examples from the area of high-frequency electronics, including broadband antennas, but also a wideband impedance transformer, and a miniaturized rat-race coupler. Analysis of the algorithm scalability with respect to the number of the search space intervals has also been considered. For each design case, the method has been thoroughly compared to a state-of-the-art multi-objective algorithm which does not rely on search space segmentation. The selected numerical results are supported by measurements of the fabricated circuit prototypes.

The future work will include application of the presented technique to a wider range of engineering problems, but also development of more efficient algorithms for identification of the intermediate points for space segmentation. Combination of the method with multi-fidelity data-driven modeling techniques such as co-kriging will be also considered.

Acknowledgement

The authors would like to thank Dassault Systemes, France, for making CST Microwave Studio available. This work was supported in part by the Icelandic Centre for Research (RANNIS) Grant 174114051, and by National Science Centre of Poland Grant 2015/17/B/ST6/01857.

References

[1] S. Chamaani, M.S. Abrishamian, S.A. Mirtaheri, "Time-domain design of UWB Vivaldi antenna array using multiobjective particle swarm optimization," *IEEE Ant. Wireless Prop. Lett.*, vol. 9, pp. 666-669, 2010.

[2] A. Bekasiewicz and S. Koziel, "A novel structure and design optimization of compact spline-parameterized UWB slot antenna," *Metrology and Measurement Systems*, vol. 23, no. 4, pp. 637-643, 2016.

[3] M.S. Khan, A.-D. Capobianco, A. Iftikhar, S. Asif, and B.D. Braaten, "A compact dual polarized ultrawideband multiple-input- multiple-output antenna," *Microw. Opt. Tech. Lett*., vol. 58, no. 1, pp. 163-166, 2016.

[4] M.G.N. Alsath and M. Kanagasabai, "Compact UWB monopole antenna for automotive communications," IEEE Trans. Ant. Prop., vol. 63, no. 9, pp. 4204-4208, 2015.

[5] L. Liu, S.W. Cheung, Y.F. Weng and T.I. Yuk "Cable effects on measuring small planar UWB monopole antennas," in M.A. Matin (ed.) *Ultra Wideband - Current Status and Future Trends*, Intech, 2012.

[6] S. Koziel and A. Bekasiewicz, *Multi-objective design of antennas using surrogate models*, World Scientific, 2016.

[7] S. Koziel and P. Kurgan, "Low-cost optimization of compact branch-line couplers and its application to miniaturized Butler matrix design," *European Microwave Conference*, Rome, pp. 227-230, 2014.

[8] T. Li, H. Zhai, G. Li, L. Li, and C. Lian,"Compact UWB band-notched antenna design using interdigital capacitance loading loop resonator," *IEEE Ant. Wireless Prop. Lett.*, vol. 11, pp. 724-727, 2012.

[9] S. Mohammadi, J. Nourinia, C. Ghobadi, J. Pourahmadazar, and M. Shokri, "Compact broadband circularly polarized slot antenna using two linked elliptical slots for C-band applications," *IEEE Ant. Wireless Prop. Lett.*, vol. 12, pp. 1094-1097, 2013.

[10] L. Wang, L. Xu, X. Chen, R. Yang, L. Han, W. Zhang, "A compact ultrawideband diversity antenna with high isolation," *IEEE Ant. Wireless Prop. Lett.*, vol. 13, pp. 35-38, 2014.

[11] A. Bekasiewicz, S. Koziel, and W. Zieniutycz, "A structure and design optimization of novel compact microscrip dual-band rat-race coupler with enhanced bandwidth," *Microwave and Optical Technology Letters*, vol. 58, no. 10, pp. 2287-2291, 2016.

[12] M.A. El Sabbagh, M.H. Bakr, and J.W. Bandler, "Adjoint higher order sensitivities for fast full-wave optimization of microwave filters," *IEEE Trans. Microw Theory Tech.*, vol. 54, pp. 3339-3351, 2006.

[13] J. Wang, X. S. Yang and B. Z. Wang, "Efficient gradient-based optimisation of pixel antenna with large-scale connections," *IET Microwaves, Antennas & Propagation*, vol. 12, no. 3, pp. 385-389, 2 28 2018.

[14] A. Bekasiewicz, and S. Koziel, "Efficient multi-fidelity design optimization of microwave filters using adjoint sensitivity," *International Journal of RF and Microwave Computer-Aided Engineering*, vol. 25, no. 2, pp. 178-183, 2015.

[15] M. Ghassemi, M. Bakr and N. Sangary, "Antenna design exploiting adjoint sensitivity-based geometry evolution," *IET Microwaves Ant. Prop.*, vol. 7, no. 4, pp. 268-276, 2013.

[16] A.J. Booker, J.E. Dennis, P.D. Frank, D.B. Serafini, V. Torczon, M.W. Trosset "A rigorous framework for optimization of expensive functions by surrogates," *Structural Optimization*, vol. 17, no. 1, pp. 1–13, 1999.

[17] M. T. Mehari *et al.*, "Efficient Identification of a Multi-Objective Pareto Front on a Wireless Experimentation Facility," in *IEEE Transactions on Wireless Communications*, vol. 15, no. 10, pp. 6662-6675, Oct. 2016.

[18] N.V. Queipo, R.T. Haftka, W. Shyy, T. Goel, R. Vaidynathan, and P.K. Tucker, "Surrogate-based analysis and optimization," *Progress in Aerospace Sciences*, vol. 41, no. 1, pp. 1-28, Jan. 2005.

[19] A.I.J. Forrester, and A.J. Keane, "Recent advances in surrogate-based optimization," Progress in Aerospace Sciences, vol. 45, pp. 50-79, 2009.

[20] S. Koziel, and J.W. Bandler, "Space mapping with multiple coarse models for optimization of microwave components," *IEEE Microw. Wireless Comp. Lett.*, vol. 18, pp. 1-3, 2008.

[21] J.W. Bandler, Q.S. Cheng, S.A. Dakroury, A.S. Mohamed, M.H. Bakr, K. Madsen, and J. Søndergaard, "Space mapping: the state of the art," *IEEE Trans. Microwave Theory Tech.*, vol. 52, no. 1, pp. 337-361, Jan. 2004.

[22] S. Koziel, S. Ogurtsov, "Model management for cost-efficient surrogate-based optimization of antennas using variable-fidelity electromagnetic simulations," *IET Microwaves Ant. Prop.*, vol. 6, no. 15, pp. 1643-1650, 2012.

[23] S. Koziel, L. Leifsson, and S. Ogurtsov, "Reliable EM-driven microwave design optimization using manifold mapping and adjoint sensitivity," *Microwave Opt. Tech. Lett.*, vol. 55, pp. 809-813, 2013.

[24] I.T. Nassar, H. Tsang, D. Bardroff, C.P. Lusk, and T.M. Weller, “Mechanically reconfigurable, dual-band slot dipole antennas,” *IEEE Trans. Ant. Prop.*, vol. 63, no. 7, pp. 3267-3271, 2015.

[25] G.L. Huang, S.G. Zhou, and T. Yuan, “Development of a wideband and high-efficiency waveguide-based compact antenna radiator with binder-jetting technique,” *IEEE Trans. Comp., Packaging Manuf. Technol*., vol. 7, no. 2, pp. 254-260, 2017.

[26] L. Liu, S.W. Cheung, and T.I. Yuk, “Compact MIMO antenna for portable devices in UWB applications,” *IEEE Trans. Antennas Prop.*, vol. 61, no. 8, pp. 4257–4264, 2013.

[27] Y. Kuwahara, “Multiobjective optimization design of Yagi–Uda antenna,” *IEEE Trans. Ant. Prop.*, vol. 53, no. 6, pp. 1984-1992, 2005.

[28] Y.M. Pan, K.W. Leung, and K. Lu, “Compact quasi-isotropic dielectric resonator antenna with small ground plane,” *IEEE Trans. Ant. Prop.*, vol. 62, no. 2, pp. 577-585, 2014.

[29] J. Liu, K.P. Esselle, S.G. Hay and S. Zhong, "Effects of Printed UWB Antenna Miniaturization on Pulse Fidelity and Pattern Stability," in *IEEE Transactions on Antennas and Propagation*, vol. 62, no. 8, pp. 3903-3910, Aug. 2014.

[30] M. Ur-Rehman, Q.H. Abbasi, M. Akram, C. Parini, “Design of band-notched ultra wideband antenna for indoor and wearable wireless communications,” *IET Microwaves, Ant. Prop.*, vol. 9, no. 3, pp. 243-251, 2015.

[31] K.R. Jha, B. Bukhari, C. Singh, G. Mishra and S.K. Sharma, "Compact Planar Multistandard MIMO Antenna for IoT Applications," in *IEEE Transactions on Antennas and Propagation*, vol. 66, no. 7, pp. 3327-3336, July 2018.

[32] Q.-X. Chu, C.-X. Mao, H. Zhu, “A Compact Notched Band UWB Slot Antenna With Sharp Selectivity and Controllable Bandwidth,” *IEEE Trans. Ant. Prop.*, vol. 61, no. 8, pp. 3961-3966, 2013.

[33] S. Koziel and A. Bekasiewicz, “Fast multi-objective surrogate-assisted design of multi-parameter antenna structures through rotational design space reduction,” *IET Microwaves, Antennas & Propagation*, vol. 10, no. 6, pp. 624-630, 2016.

[34] C.-H. Tseng, and C.-L. Chang, “A rigorous design methodology for compact planar branch-line and rat-race couplers with asymmetrical T-structures,” *IEEE Trans. Microw. Theory Techn*. vol. 60, no. 7, pp. 2085–2092, 2012.

[35] C.-H. Tseng, and H.-J. Chen, “Compact Rat-Race Coupler Using Shunt-Stub-Based Artificial Transmission Lines,” *IEEE Microw. Wireless Comp. Lett.*., vol. 18, no. 11, pp. 734-736, 2008.

[36] A. Bekasiewicz and P. Kurgan, “A compact microstrip rat-race coupler constituted by nonuniform transmission lines,” *Microwave Opt. Tech. Lett.*, vol. 56, no. 4, pp. 970-974, 2014.

[37] K. Deb, *Multi-Objective Optimization Using Evolutionary Algorithms.* New York, NY, USA: Wiley, 2001.

[38] S. Koziel, and S. Ogurtsov, “Multi-objective design of antennas using variable-fidelity simulations and surrogate models,” *IEEE Trans. Ant. Prop.*, vol. 61, no. 12, pp. 5931-5939, 2013.

[39] X.-S. Yang, K.T. Ng, S.H. Yeung, K.F. Man, “Jumping Genes Multiobjective Optimization Scheme for Planar Monopole Ultrawideband Antenna,” *IEEE Trans. Ant. Prop.*, vol. 56, no. 12, pp. 3659-3666, 2008.

[40] C.A. Coello Coello, G.B. Lamont, and D.A. van Veldhuizen, *Evolutionary algorithms for solving multi-objective problems*, 2nd ed, Springer-Verlag, New York, 2007.

[41] H. Choo, R.L. Rogers, H. Ling, “Design of electrically small wire antennas using a Pareto genetic algorithm,” *IEEE Trans. Ant. Prop.*, vol. 53, no. 3, pp. 1038-1046, 2005.

[42] N. Jin and Y. Rahmat-Samii, “Advances in particle swarm optimization for antenna designs: real-number, binary, single-objective and multiobjective implementations,” *IEEE Trans. Ant. Prop*., vol. 55, no. 3, pp. 556-567, 2007.

[43] R. Li, L. Xu, W. Hu, Y.Z. Yin and X.W. Shi, "Low-cross-polarisation synthesis of conformal antenna arrays using a balanced dynamic differential evolution algorithm," in *IET Microwaves, Antennas & Propagation*, vol. 11, no. 13, pp. 1853-1860, 10 20 2017.

[44] P. Baumgartner *et al*., "Multi-Objective Optimization of Yagi–Uda Antenna Applying Enhanced Firefly Algorithm With Adaptive Cost Function," in *IEEE Transactions on Magnetics*, vol. 54, no. 3, pp. 1-4, March 2018.

[45] L. dos Santos Coelho, T.C. Bora, F. Schauenburg and P. Alotto, "A Multiobjective Firefly Approach Using Beta Probability Distribution for Electromagnetic Optimization Problems," in *IEEE Transactions on Magnetics*, vol. 49, no. 5, pp. 2085-2088, May 2013.

[46] D.E. Goldberg and J. Richardson, “Genetic algorithms with sharing for multimodal function optimization,” Proc. Int. Conf. Genetic Algorithms App., pp. 41–49, Hillsdale, 1987.

[47] S.L. Ho and S. Yang, "Multiobjective Synthesis of Antenna Arrays Using a Vector Tabu Search Algorithm," in *IEEE Antennas and Wireless Propagation Letters*, vol. 8, pp. 947-950, 2009.

[48] B. Aljibouri, A. Sambell, and B. Sharif, "Application of genetic algorithm to design of sequentially rotated circularly polarised dual-feed microstrip patch antenna array," *Electronics Lett.*, vol. 44, no. 12, pp. 708–709, 2008.

[49] S. Koziel and A. Bekasiewicz, "Rapid simulation-driven multiobjective design optimization of decomposable compact microwave passives," *IEEE Transactions on Microwave Theory and Techniques*, vol. 64, no. 8, pp. 2454-2461, 2016.

[50] T.W. Simpson, J.D. Pelplinski, P.N. Koch, and J.K. Allen, "Metamodels for computer-based engineering design: survey and recommendations", *Engineering with Computers*, vol. 17, pp. 129-150, 2001.

[51] S. Koziel, A. Bekasiewicz, I. Couckuyt, and T. Dhaene, "Efficient multi-objective simulation-driven antenna design using co-kriging," *IEEE Transactions on Antennas and Propagation*, vol. 62, no. 11, pp. 5900-5905, 2014.

[52] S. Koziel, A. Bekasiewicz, and W. Zieniutycz, "Expedited EM-driven multi-objective antenna design in highly-dimensional parameter spaces," *IEEE Antennas and Wireless Propagation Letters*, vol. 13, pp. 631-634, 2014.

[53] S. Koziel and A. Bekasiewicz, "Fast multiobjective optimization of narrowband antennas using RSA models and design space reduction," *IEEE Antennas and Wireless Propagation Letters*, vol. 14, pp. 450-453, 2015.

[54] S. Koziel and A. Bekasiewicz, "Domain segmentation for low-cost surrogate-assisted multi-objective design optimization of antennas," to appear, *IET Microwaves, Antennas & Propagation*, 2018.

[55] S. Koziel, A. Bekasiewicz, and S. Szczepanski, "Multi-objective design optimization of antennas for reflection, size and gain variability using kriging surrogates and generalized domain segmentation," *International Journal of RF and Microwave Computer-Aided Engineering*, vol. 28, no. 5, pp. 1-11, 2018.

[56] A. Bekasiewicz and S. Koziel, "Miniaturized uniplanar triple-band slot dipole antenna with folded radiator," *Microwave and Optical Technology Letters*, vol. 60, no. 2, pp. 386-389, 2018.

[57] A. Bekasiewicz, S. Koziel, and B. Pankiewicz, "Accelerated simulation-driven design optimisation of compact couplers by means of two-level space mapping," *IET Microwaves, Antennas & Propagation*, vol. 9, no. 7, pp. 618-626, 2015.

[58] K. Tan, E. Khor, and T. Lee, *Multiobjective Evolutionary Algorithms and Applications*, series Advanced Information and Knowledge Processing. London: Springer, 2005.

[59] A.I. Forrester, A. Sobester, and A.J. Keane, *Engineering Design via Surrogate Modelling: A Practical Guide*. Chichester: John Wiley & Sons, 2008.

[60] D. Gorissen, I. Couckuyt, E. Laermans, et al. "Multiobjective global surrogate modeling, dealing with the 5-percent problem," *Engineering with Computers*, vol. 26, no. 1, pp. 81-98, 2010.

[61] B. Beachkofski and R. Grandhi, "Improved distributed hypercube sampling," *American Institute of Aeronautics and Astronautics*, paper AIAA 2002-1274, 2002.

[62] P. Kurgan, A. Bekasiewicz, and M. Kitlinski, "On the low-cost design of abbreviated multi-section planar matching transformer," *Microwave and Optical Technology Letters*, vol. 57, no. 3, pp. 521-525, 2015.

[63] CST Microwave Studio, ver. 2013, Dassault Systems, 10 rue Marcel Dassault, CS 40501, Vélizy-Villacoublay Cedex, France, 2013.

[64] Sonnet, ver. 14.54, Sonnet Software, Elwood Davis Road 100, North Syracuse, NY 13212, 2013.

[65] P.D. Hough, T.G. Kolda, and V.J. Torczon, "Asynchronous parallel pattern search for nonlinear optimization," *SIAM J. Sci. Comput.*, vol. 23, no. 1, pp. 134–156, 2001.

[66] Palaniswamy, S.K., Panneer, Y., Nabi Alsath, M.G., Kanagasabai, M., Kingsly, S., Subbaraj, S.: "3D eight-port ultra-wideband (UWB) antenna array for diversity applications," *IEEE Ant. Wireless Prop. Lett.*, 2016.

[67] A. Conn, N.I.M. Gould, P.L. Toint, *Trust-region methods*, MPS-SIAM Series on Optimization, Philadelphia, 2000.

[68] M.A. Haq, S. Koziel, and Q.S. Cheng, "EM-driven size reduction of UWB antennas with ground plane modifications," *Int. Applied Computational Electromagnetics Society (ACES China) Symposium*, 2017.